OBSERVATION OF THE INTERACTION BETWEEN A TRANSONIC SHOCK WAVE AND A WINGTIP VORTEX

by

TROY T BUSHMIRE

Presented to the Faculty of the Graduate School of

The University of Texas at Arlington in Partial Fulfillment

of the Requirements

for the Degree of

MASTER OF SCIENCE IN AEROSPACE ENGINEERING

THE UNIVERSITY OF TEXAS AT ARLINGTON

December 2018

Acknowledgements

I would like to thank Dr. Frank Lu for the opportunity work with him and for advising me throughout all of my Master's thesis work. I would also like to thank the rest of my Master's thesis committee members: Dr. Donald Wilson and Dr. Zhen Han. This has been a tremendous learning experience for me.

Further, I would specifically like to thank Dr. James Grisham for all of his help getting FUN3D installed on the Texas Advanced Computing Center's (TACC) Lonestar 5. In addition I would like to thank the whole TACC team for providing assistance throughout this installation. David Carter also provided assistance with this installation, as well as assisting me with all Pointwise related issues.

I would like to thank Bell for providing tuition assistance to allow me to attend The University of Texas at Arlington to pursue a Master's degree in Aerospace Engineering. I would also like to thank UTA for being so accommodating for distance learning students. Without the support of both Bell and UTA, none of this would have been possible.

Further, I would like to thank my family: My parents for raising me and supporting me in achieving my academic goals; my wife for all the extra work she has done for our family to allow me to pursue a Masters degree.

Abstract

OBSERVATION OF THE INTERACTION BETWEEN TRANSONIC SHOCK WAVE AND WINGTIP VORTEX

Troy Bushmire, MS

The University of Texas at Arlington, 2018

Supervising Professor: Frank Lu

The present study observes the interaction between two fundamental phenomena in fluid mechanics: the transonic shock wave and the wingtip vortex. While these are two areas of fluid mechanics in which extensive experimental and numerical research has been conducted, there is little information on the interaction between the two. The present study numerically simulates a wing with a NACA-0012 section at Mach 0.758 and observes the interaction between the transonic shock wave and wingtip vortex for various angles of attack. The focus of the study is on the surface flow topology and the flow exterior to the boundary layer. Results show interesting surface flow topology for cases in which shock-induced separation occurs. Lines of separation and reattachment converge smoothly near the wingtip with no evidence of singular point, identifying a region of open separation. Results on the outer flow show there is a distinct interaction between the wingtip vortex and the transonic shock wave. The relationship is directly related to the regions of supersonic and subsonic flow. It is shown that, in general the wingtip vortex only affects regions of subsonic flow.

Table of Contents

List of Illustrations

List of Tables

Nomenclature

a	speed of sound
C_p	coefficient of pressure
γ	specific heat ratio
L	reference length
M	Mach number
P	static pressure
P_t	total press
$P_{T_{BC}}$	total pressure ratio boundary condition
$P_{T_{plenum}}$	total pressure in tunnel test section
P_∞	static pressure in tunnel test section
ρ	density
ρ_t	total density
ρ_w	wall density
R	universal gas constant
Re	Reynolds number
S	Sutherland's constant
T	static temperature
T_t	total temperature
$T_{T_{BC}}$	Total temperature ratio boundary condition
$T_{T_{plenum}}$	total temperature in tunnel test section
T_∞	static temperature in tunnel test section

T_{ref}	reference temperature
τ_w	shear stress at wall
U	freestream velocity
μ	Dynamic viscosity
μ_τ	friction velocity
μ_{ref}	Reference dynamic viscosity
ν	Kinematic viscosity
y	dimensional initial spacing from wall

Chapter 1 : Introduction

The study of transonic flow using computational fluid dynamics (CFD) has been at the forefront of aerospace engineering. The transonic flow regime is particularly of interest due to its relevance in a wide range of aircraft, considering that significant percentage of both commercial and military aircraft fly in this regime. Moreover, supersonic and hypersonic aircraft, as well as space launch vehicles have to negotiate the transonic regime to attain their operational regimes. By definition, a transonic flow regime is one with mixed subsonic and supersonic pockets. This type flow most likely will involve shock waves, the location of which is difficult to predict primarily due to their interaction with the boundary layer. Shock/boundary-layer interactions (SBLIs) constitute a class of fluid mechanics problems that is of great practical significance. SBLIs create very complex flow structures particularly when the boundary layer is separated. Numerous adverse effects occur when the flow separates. In the transonic regime, some of these include increase drag and larger flow unsteadiness known as buffeting.

The desire for detailed understanding of the transonic flow regime has inspired great leaps forward in computational fluid dynamics. This has not only made solving transonic regime problems faster and more accurate, but also made solving complex problems possible. A large part of aerodynamics research that requires advanced CFD capability is related to turbulence modeling. In general, Reynolds-Averaged Navier-Stokes (RANS) models are most popular within the aerospace industry. This is due to their ability to provide reasonable results at a relatively low computational cost. At the forefront of CFD is Direct Numerical Simulation (DNS). DNS solves the full Navier-Stokes equations without the implementation of a turbulence model. However, it still requires a model for the very small turbulent structures. While DNS is extremely accurate for solving

flowfields numerically, the computational requirement is currently too high to be used for most practical applications.

CFD is most widely used as an engineering tool to analyze an aircraft's performance; however, it is also an excellent tool for the study of fluid phenomena. The goal of the present study is to observe and understand the topological flow features on a finite wing with a NACA-0012 profile in transonic flow. In particular, observations of the complex transonic shock wave interaction with wingtip vortices are made. The present study conducts a qualitative assessment of two flow phenomena, wingtip vortices and shock waves. These two phenomena arise in transonic aerodynamics and are relatively well understood on their own. However, their mutual interaction is still a topic to be investigated. While of fundamental interest, this study finds application in transonic buffeting and flutter, and their control.

The present study was conducted via CFD in lieu of experiment for a few reasons. The first is the ease and accessibility of CFD compared to experiments. The second reason is the vast options of post-processing tools available to visualize the flow.

The nature of the present study is not to obtain detailed and accurate data or for engineering design. This study instead aims to qualitatively observe the physics at play and gain an understanding of surface topology as well as the interaction between transonic shock waves and wingtip vortices. For these reasons, it was deemed sufficient to use a RANS turbulence model, specifically the $k-\omega$ SST model. Steady RANS with the $k-\omega$ SST model greatly reduced computational time. The ability of RANS models to provide reasonable results, even for complex flow structures found in SBLI problems, is further justified through the work by Viera et al. [1]

Chapter 2 : Modeling Numeric Simulations

All numerical simulations carried out utilized five separate software packages for geometry development, mesh generation, computations and post processing. Geometry was developed using CATIA® V5 software. All mesh generation was done using Pointwise®. Meshes were three-dimensional and unstructured. Surface meshes were made up of triangular elements and while volume meshes contained prism, tetrahedral, and pyramidal cells. NASA's FUN3D was utilized as the solver. Solutions were carried out using FUN3D's three-dimensional pseudo-transient node-based finite volume discretization scheme [2]. As suggested by NASA in [2], simulations utilized one CPU core per 50,000 grip points. Post-processing was done using FieldView®. Geometry creation, mesh generation and post processing were carried out on a local desktop computer whereas solutions with NASA's FUN3D were carried out on the Texas Advanced Computing Center's (TACC) machine Lonestar 5. Information for gaining student access to both Pointwise and to TACC resources is available in Appendix A.

2.1 : Empty Tunnel Mesh

Three separate meshes were used to throughout this study. The first was a model of an empty NASA Langley 8-foot pressure wind tunnel. This wind tunnel was the facility used in the work of Harris [3] and was numerically simulated in the present study. This specific study was chosen because it contained experimental results without the use of transition strips and data was presented without any wall corrections. This makes it easier to compare with CFD. The purpose of simulating the empty tunnel was to tune pressure boundary conditions at the tunnel inlet and outlet to achieve the desired flow conditions in the test section where the present study was carried out. The empty tunnel model, shown in Figure 1 was composed of three discrete sections: the contraction section, the test section and the diffuser section.

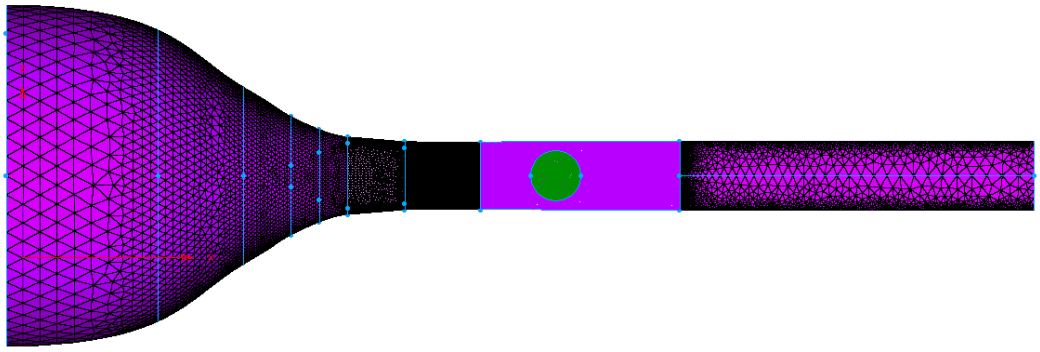

Figure 1: Empty Tunnel Mesh

The contraction section and test section were modeled to replicate the physical tunnel geometry and thus flow conditions of the actual tunnel. Dimensions for these geometries are available from [4]. A notable discrepancy between the model and the physical tunnel is the test section walls. The NASA Langley tunnel was equipped with a sophisticated set of slots in the walls to maintain the desired Mach number throughout the test section. For the sake of simplicity, the present model used plain, solid walls. The diffuser section geometry was created by elongating the test section. This was considered to be a numerical diffuser and its purpose was to provide a coarse mesh to dissipate any wakes originating from the test article (once it was placed in the tunnel). Wake interaction with the tunnel outlet pressure boundary can create solution convergence issues.

Throughout the present study, inviscid boundary conditions were applied at the tunnel walls. The main areas of focus are near or on the centerline of the wind tunnel; thus the inviscid boundary condition is justified. This greatly reduces the cell count of the mesh, as there is no need to resolve the tunnel wall boundary layers. The empty tunnel mesh consisted of 644,590 nodes and 3,602,056 cells. A breakdown of the node and cell

counts is provided in Table 1. Since there was no boundary layer to be resolved, no limit on wall initial spacing was imposed.

Table 1: Node and cell count breakdown for empty tunnel mesh

Tunnel Section	Nodes	Cells
Contraction Section*	92,187	476,947
Test Section	526,339	3,002,291
Diffuser Section*	26,064	122,818

*Remains the same throughout all meshes

2.2 : Two-Dimensional Mesh

The second mesh was built upon the first with the inclusion of an airfoil section spanning the entire width of the tunnel. The airfoil geometry definition was set based on a test described by Harris [3]. This test article was a NACA 0012 airfoil section with a 25 in chord that spanned the entire width of the test section. The airfoil in test section mesh is illustrated in Figure 2.

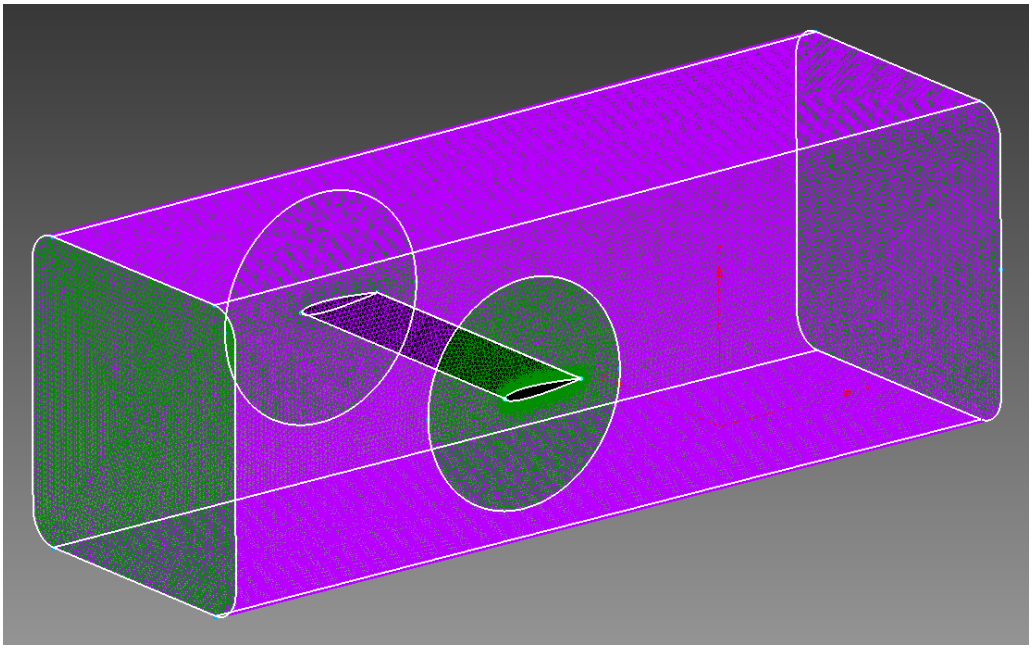

Figure 2: Surface mesh for the test section with airfoil section inside

While Figure 2 shows only the test section of the mesh, the actual simulation included the contraction and diffuser section as shown in Figure 1. By breaking up the wind tunnel mesh into the three sections (contraction, test and diffuser), only the test section mesh required updating throughout all simulations within the present study. It is noted that the green circle around the airfoil section has its center-line axis at the airfoil quarter chord. To change angle of attack, the airfoil is rotated about this axis; only the green circle mesh needs to be regenerated.

For all viscous surface simulated in the present study (airfoil and wing surfaces) a $y^+ = 1$ was implemented, where

$$y^+ = \frac{yu_\tau}{\nu} \quad [1]$$

and where y is the dimensional initial spacing from the wall, ν is the kinematic viscosity and

$$u_\tau = \sqrt{\frac{\tau_w}{\rho_w}} \quad [2]$$

is the friction velocity. In Equation [2] τ_w is the shear stress at the wall and ρ_w is the wall density.

The original two-dimensional mesh contained 5,563,894 nodes and 8,994,064 cells. Of these, 5,445,643 nodes and 8,975,896 cells existed in the test section portion of the mesh. For the grid resolution study, the goal was to double the resolution of the mesh. This mesh yielded 10,513,905 points and 17,563,619 cells within the test section.

2.3 : Three-Dimensional Mesh

The final set of meshes developed was for the three-dimensional case of the wingtip, the focus of the present study. The geometry was developed by cutting the two-dimensional geometry in half, precisely at the tunnel vertical axis and blending in the

upper and lower surfaces of the NACA 0012 with a half-body surface of revolution. This can be seen in Figure 3.

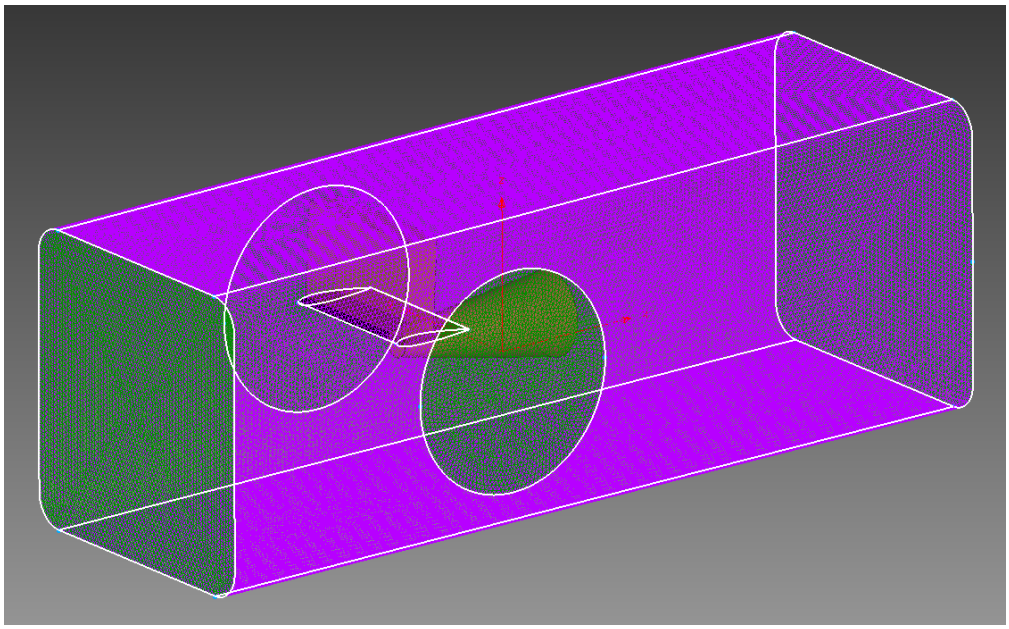

Figure 3: Surface mesh for test section with wing

The 3^0 angle of attack case is illustrated in Figure 3. The meshes for the remaining angles of attack had identical surface meshes (other than the wing surface being rotated), the only difference being in the generation of the volume mesh.

With the inherently more complex flow field associated with the three-dimensional case, a more involved grid refinement was required. A powerful tool within Pointwise® known as “sources” was utilized. Sources are three-dimensional structures rigged in space in which volume mesh modifications can be made. Two sources were used for each of the three-dimensional grids:

- Wing tip source – used to increase grid resolution around the wing tip to better capture wing tip vortices

- Shock wave source – large box along the entire span of the wing from about 5-50% chord used to increase mesh resolution where shocks are expected to be

Both of these sources can be seen in Figure 3. Given the relatively simple shock wave structure expected in the present study, it was decided to use a shock wave source in lieu of implementing an adaptive mesh feature within the solver. The term “relatively simple” refers to the fact the shock wave’s general location is easy to predict, and no reflected shock waves are expected. This greatly simplifies the solution portion of the study. Figure 4 illustrates how the sources provide a denser mesh distribution in areas that shock and complex viscous effects are expected to be present.

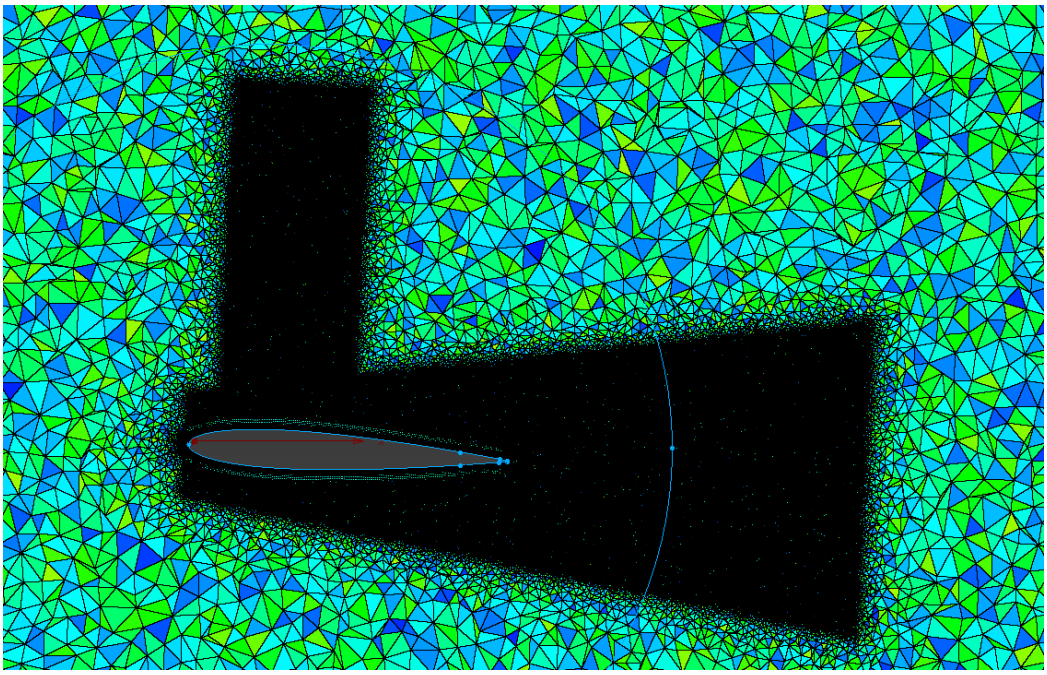

Figure 4: Cross-sectional cut of volume mesh near the wingtip

One may expect the surface node counts for the three-dimensional case to be close to half of that of the two-dimensional case. However, by increasing surface mesh resolution, greater shock wave resolution can be achieved. This was not required for two-

dimensional interactions where the absence of the third dimension yielded simpler flow structures. On the other hand, complex structures exist in three dimensional cases especially at higher angles of attack. The reason for the surface mesh resolution's effect on volume mesh resolution stems from how Pointwise® was utilized. For volume mesh generation, prism layers were grown from the surface up until the point that an isotropic tetrahedral cell could be created as illustrated in Figure 5. It can be seen that by shrinking the size of the initial surface cell, the size of the cell will also be smaller once isotropy is reached. This yielded more resolution within the boundary layer (and in general near the surface) which is very desirable for problems dealing with shock wave-boundary layer interaction.

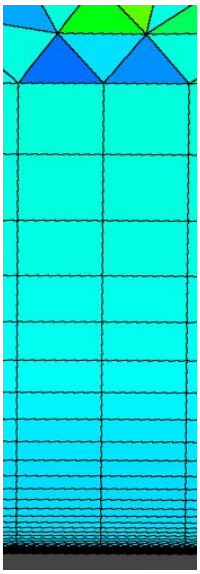

Figure 5: Prism layer transition to tetrahedral cells

The node and cell counts for each of the three-dimensional meshes are provided below in Table 2.

.

Table 2: Node and cell count breakdown for three-dimensional meshes

Angle of Attack (º)	Test Section Node Count	Test Section Cell Count
0	17,178,413	75,154,328
0.14	16,015,753	68,173,441
1	16,015,714	68,175,152
3	17,175,855	75,134,975
5	16,014,338	68,166,694

.

Chapter 3 : Results and Discussion

3.1 : Empty Tunnel

In order to obtain useful data for the present study, a sufficient model of the wind tunnel and flow conditions was required. This was done using an empty wind tunnel model. The goal was to duplicate tunnel conditions such that the pertinent data of [3] could be replicated numerically. This would verify the numerical approach and the topic of the present study could be carried out with confidence.

In [3], tests were conducted at several Mach and Reynolds numbers. The conditions of interest for the present study were a Mach number of 0.758 and a Reynolds number of 3 million. It can be noted that the reference length is the specimen's chord. From [4], typical operating total temperatures for the 8-foot NASA Langley Pressure Tunnel were between 100-120ºF. For this study, a total temperature of 110ºF was assumed.

The Mach number, Reynolds number and total temperature were known from [3,4]. From here, a series of calculations was carried out to fill out the rest of the unknown flow parameters, such as:

$$\frac{T}{T_t} = \left(1 + \frac{\gamma - 1}{2} M^2\right)^{-1} \quad [3]$$

$$a = \sqrt{\gamma R T} \quad [4]$$

$$M = \frac{a}{U} \quad [5]$$

$$\mu = \mu_{ref} \left(\frac{T}{T_{ref}}\right)^{\frac{3}{2}} \frac{T_{ref} + S}{T + S} \quad [6]$$

$$R_e = \frac{\rho U L}{\mu} \quad [7]$$

$$\frac{\rho}{\rho_t} = \left(1 + \frac{\gamma - 1}{2} M^2\right)^{\frac{-1}{\gamma - 1}} \quad [8]$$

$$P = \rho R T \quad [9]$$

$$\frac{P}{P_t} = \left(1 + \frac{\gamma - 1}{2} M^2\right)^{\frac{-\gamma}{\gamma - 1}} \quad [10]$$

- Equation 3 – Isentropic relation for temperature, used to calculate static temperature, T.
- Equation 4 – Used to calculate speed of sound, a.
- Equation 5 – Mach number equation, used to calculate airspeed, U.
- Equation 6 – Sutherland's Law, used to calculate dynamic viscosity, μ
- Equation 7 – Reynolds number equation, used to calculate density, ρ
- Equation 8 – Isentropic relation for density, used to calculate stagnation density, ρ_t
- Equation 9 – Ideal Gas Law, used to calculate static pressure, P
- Equation 10 – used to calculate total pressure, P_t

Table 3 summarizes the test section flow field values calculated and used for the present study.

Table 3: Test section flow field parameters

Parameter	Symbol	Value	Units
Reynolds Number	R_e	3.00×10^6	Non-Dimensional
Mach Number	M	0.758	Non-Dimensional
Speed of Sound	a	1108	ft/s
Kinematic Viscosity	ν	3.74×10^{-7}	ft^2/s
Incoming Airspeed	U	840	ft/s
Temperature	T	51	ºF
Stagnation Temperature	T_t	110	ºF
Pressure	p	562	psia
Stagnation Pressure	p_t	823	psia
Density	ρ	6.41×10^{-4}	$slug/ft^3$
Stagnation Density	ρ_t	8.41×10^{-4}	$slug/ft^3$

With the key flow parameters calculated, the simulation could be carried out. Since there are contractions and expansions through the various stream-wise cross-sections of the numerical tunnel model, airspeed and thus Mach number varied throughout the length of the tunnel, specifically the test section (without the use of sophisticated slots to maintain constant Mach number). For this reason, the station location corresponding to the quarter chord of where the test article would be placed was chosen as the reference location to obtain a Mach of 0.758. This was the location of the aerodynamic center for both the airfoil and wing section, making it the most significant physical location in the tunnel to match the Mach number.

FUN3D allows for the direct input of static temperature, Mach number as well as Reynolds number per grid unit. To achieve the flow conditions outlined in Table 3, a total pressure ratio and a total temperature ratio as boundary conditions at the tunnel inlet and a static pressure ratio at the tunnel outlet were required. The equations for these two boundary conditions are:

$$P_{T_{BC}} = \frac{P_{t_{plenum}}}{P_{\infty}} \quad [11]$$

$$T_{T_{BC}} = \frac{T_{t_{plenum}}}{T_{\infty}} \quad [12]$$

respectively where $P_{t_{BC}}$ is the total pressure ratio boundary condition, $P_{t_{plenum}}$ is the total pressure and p_{∞} is the static pressure in the test section. The same subscripts apply to Equation 12 for the total temperature ratio.

The final boundary condition, static pressure ratio at the outlet, was developed via an iterative process. The initial guess for the static pressure ratio was the ratio between the cross-sectional area of the wind tunnel inlet and the wind tunnel outlet.

With the boundary conditions at the inlet imposed, and the initial guess of outlet boundary condition made, the solver was executed and results were analyzed. This

process was repeated, varying the static pressure ratio at the outlet until the goal of Mach 0.758 at the wing quarter chord station location was achieved. Figure 6.a. shows the Mach number distribution throughout the length of the tunnel and Figure 6.b. shows a cross-section cut at the test article quarter chord plane with a more refined Mach number distribution.

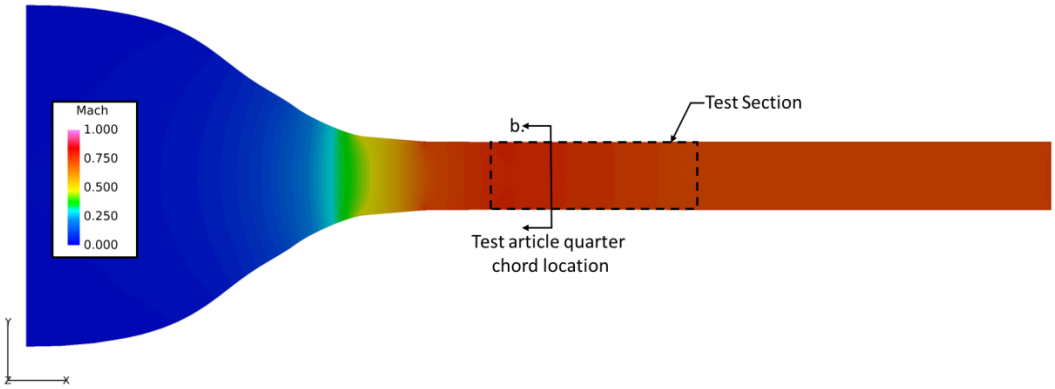

a. Whole Tunnel Mach Distribution

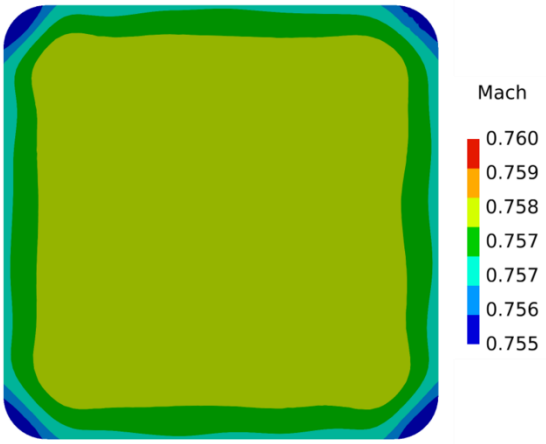

b. Detailed Mach Distribution at location of test article quarter chord

Figure 6: Empty tunnel Mach number distribution

3.2 : Two-Dimensional Study

The goal of the two-dimensional verification study was to demonstrate that the meshing quality was sufficient. By replicating experimental data, deviations to the verified model can be made confidently to explore new flow phenomena in the present study. This part of the study directly simulated one of the test cases of [3] for a NACA 0012 airfoil at Mach 0.758 as summarized in Table 4. A desirable feature of the data was that no transition strips were used on the test article. This made it more effective for validating numerical simulations.

Table 4: Summary of two-dimensional experiment parameters

Airfoil	NACA-0012
Span	85.75 in (entire width of tunnel)
Chord	25 in
Mach	0.758
Angle of attack	-0.14º
Reynolds Number	3 million

The convergence criteria used throughout this study were as follows:

- All residuals must drop at least four orders of magnitude
- Lift and drag forces must not vary more than 0.1% over the last 10% of the iterations

Once unsteady phenomena occur and force results oscillate with iterations the second criterion becomes harder or impossible to satisfy. For those cases, referencing residuals in combination with engineering judgement were used to verify solution convergence. Figure 7 and Figure 8 illustrate that both these criteria were satisfied for the two-dimensional verification study. Figure 7 shows the desired fourth-order drop in residuals for all residuals. Figure 8 shows convergence of both drag and lift.

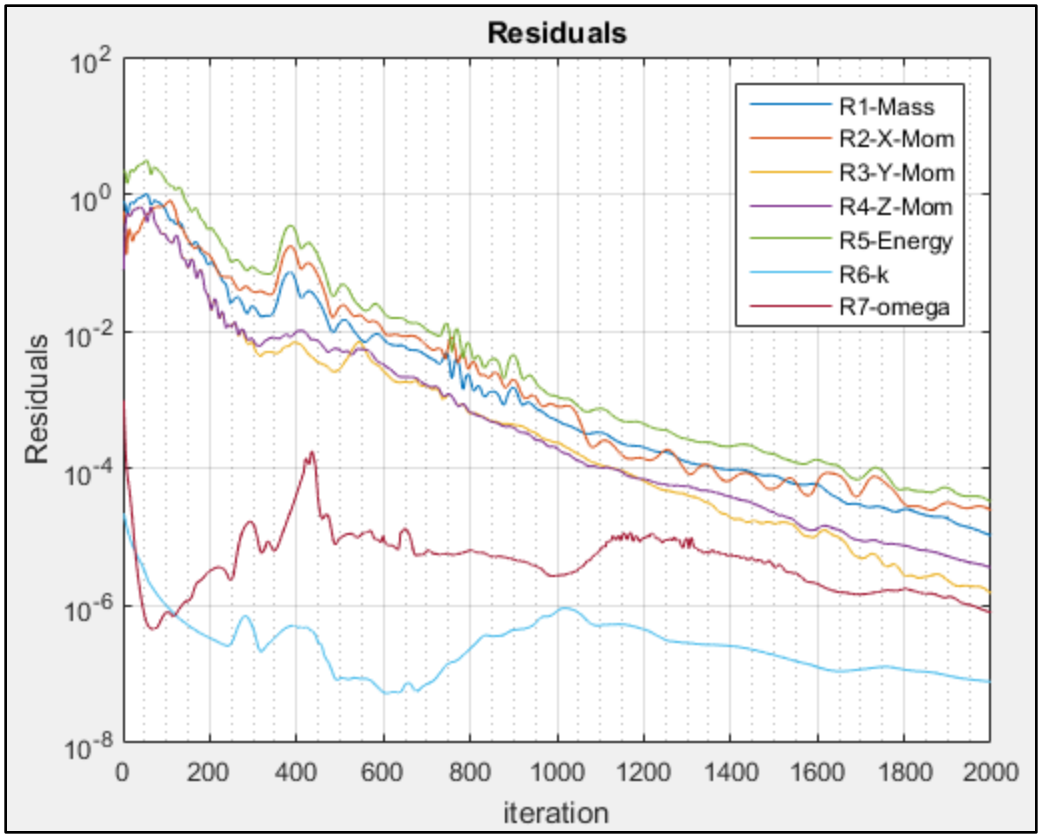

Figure 7: Residuals vs. iteration for two-dimensional verification study

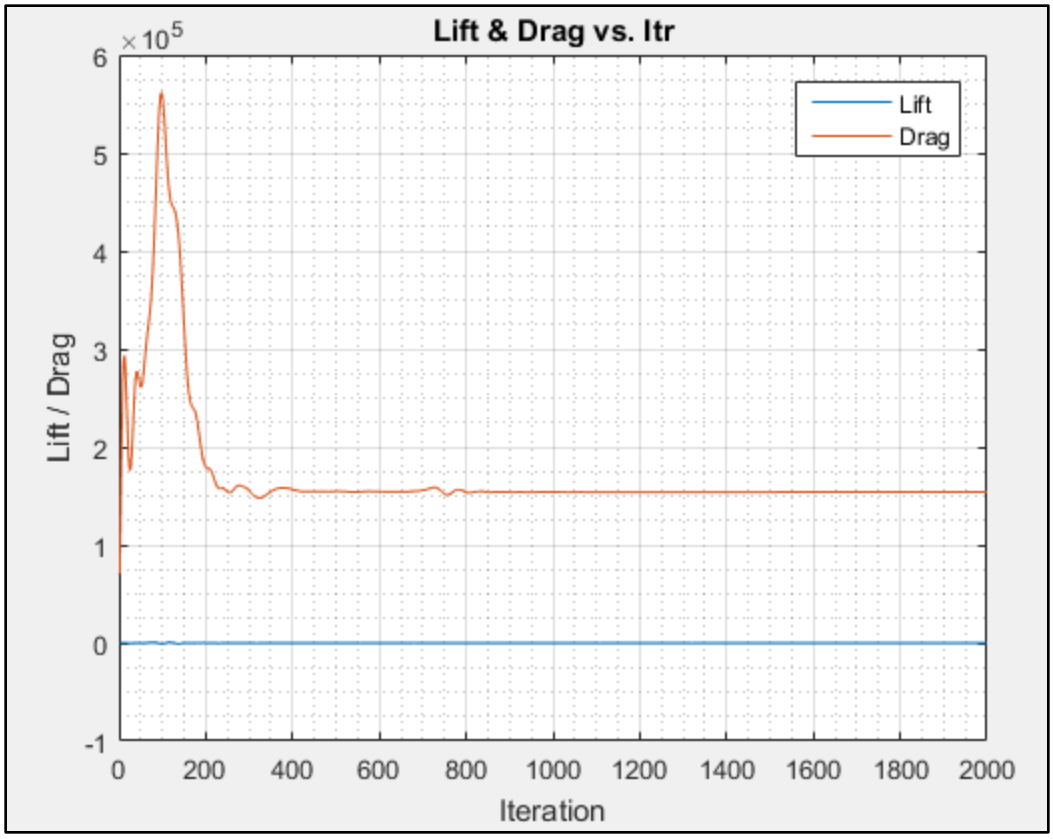

Figure 8: Lift and drag vs. iteration for two-dimensional verification study

With convergence verified, post processing was carried out by analyzing pressure distributions along the airfoil. To be consistent with [3], section cuts were taken 8 inches to the left of the centerline of the airfoil. Before comparing the numerical results to experiment, a grid resolution study was conducted to ensure that the results were not grid dependent. This was done by doubling the grids of the two-dimensional mesh and comparing chord-wise pressure distributions at the desired location. Results of the grid resolution study, in the form of airfoil C_p-distributions, are presented in Figure 9. Figure 9 verifies that the solution is unchanged with a doubling of the grid resolution implying that the results were not grid dependent. Numerical results were then compared to experiment in Figure 10.

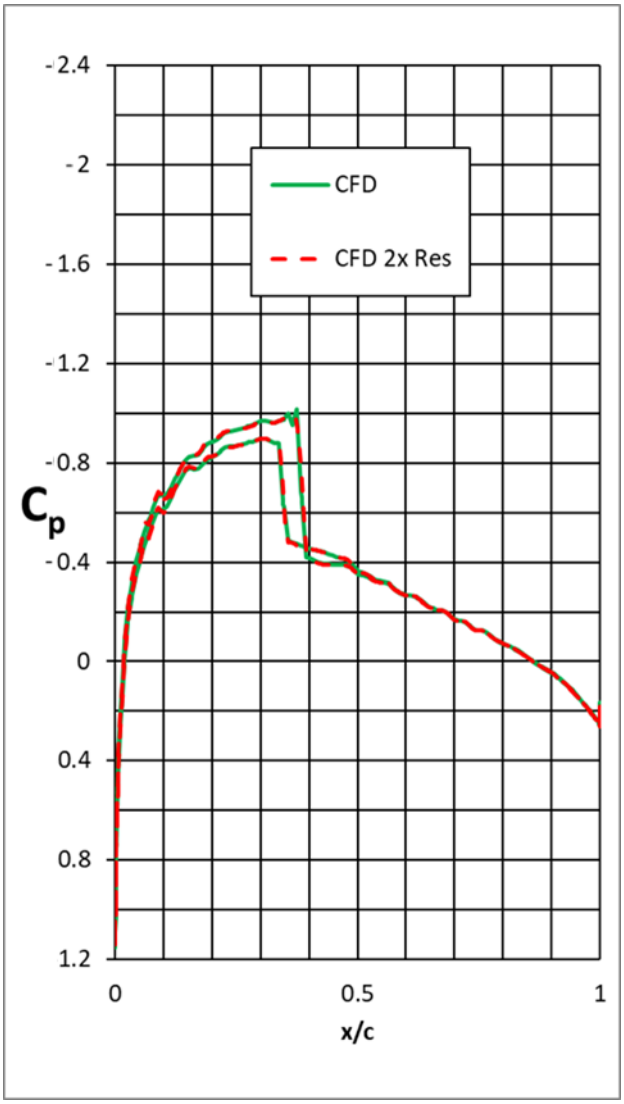

Figure 9: Chord-wise pressure distribution of airfoil section at Mach 0.758

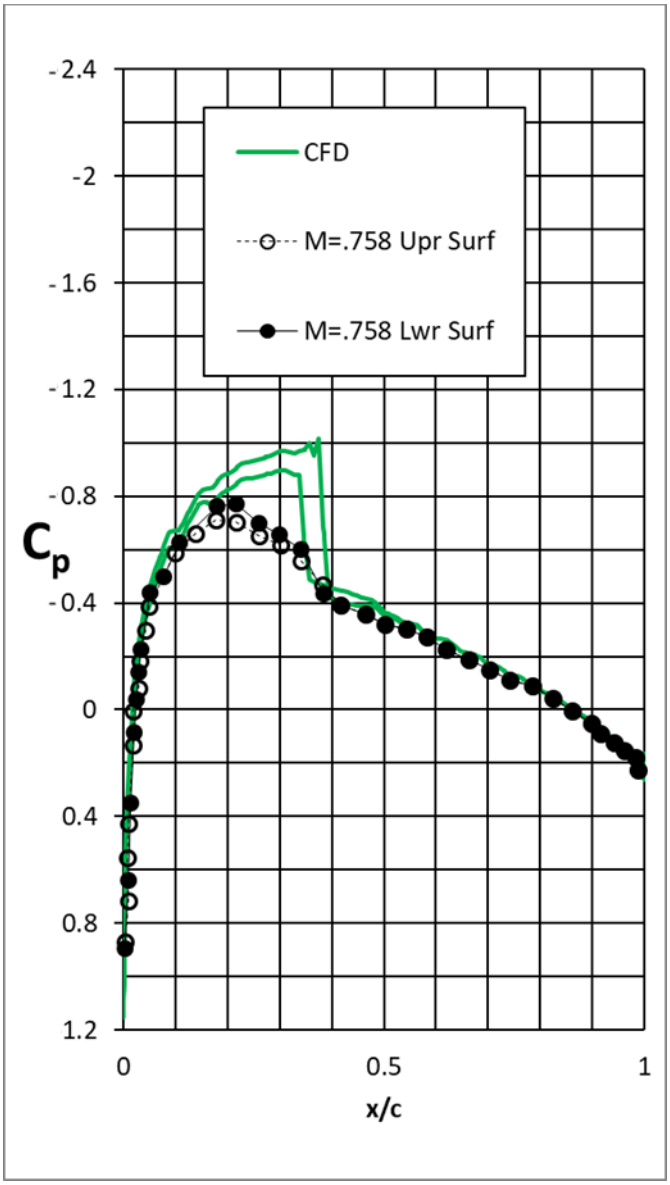

Figure 10: Experimental and numerical chord-wise C_p distribution for airfoil section at Mach 0.758

Figure 10 shows that while the numerical simulation accurately predicted the shock location on the airfoil, it missed the C_p magnitudes forward of the shock. At first glance this seems concerning. There are a few points to note:

1. Recall that one of the discrepancies between the numerical and the experimental conditions was maintaining a constant Mach number throughout the test section. It is well known that transonic test data are sensitive to wall conditions [8,9]. While a sophisticated slotted wall arrangement was implemented in the experiment, the numerical simulation utilized a simple wall boundary condition. However, this difference is a possible reason for the discrepancy.
2. The boundary conditions used in the empty tunnel were used directly in the two-dimensional simulation. The presence of the airfoil in the tunnel would inherently cause a blockage in the tunnel, given the same initial boundary conditions this could yield slightly different freestream Mach numbers compared to the empty tunnel case.

These are believed to be the causes for the discrepancy between experimental and numerical results. To verify this conjecture, the numerical data were instead compared to the experimental data gathered at Mach 0.779 in Figure 11.

Results from Figure 11 appear to agree better with experimental data. The two-dimensional study aimed to match a Mach number of 0.758. Thus it is fair to say that these two cases presented in Figure 11 are actually more analogous to each other. This supports the theory that using the same boundary conditions as the empty tunnel case with a blockage in the tunnel (the airfoil section) is altering the effective freestream Mach number. The main point to highlight is the fact that the numerical simulation seems to do a sufficient job in predicting shock location. The results were deemed sufficient to move on to the three-dimensional simulations, the focus of this study.

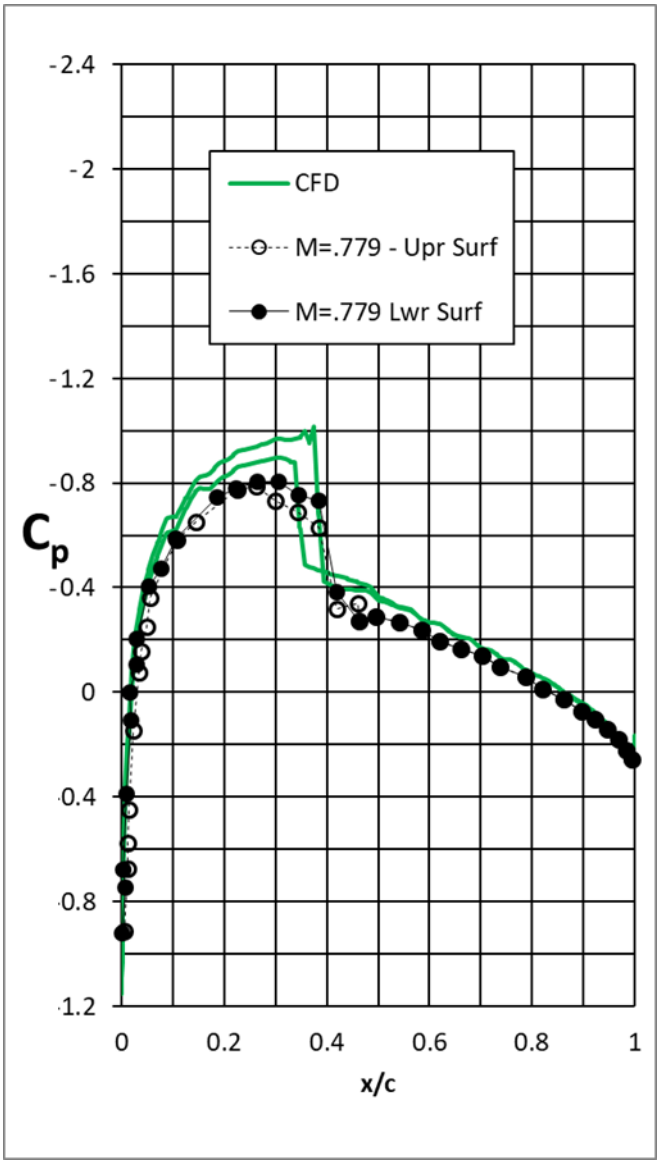

Figure 11: Chord-wise C_p distribution along NACA-0012 airfoil section, Experimental data at Mach 0.779 and Numerical data at Mach 0.758

3.3 : Three-Dimensional Study

After fine tuning boundary conditions and verifying the mesh quality, the study at hand could be carried out. An angle of attack sweep of the finite wing was run from 0º to 5º in the following increments: 0º, 0.14º, 1º, 3º, 5º. This was determined to be a

reasonable range of angle of attacks to analyze. The 0.14º case was chosen for two reasons: the first was to have some comparison to the two-dimensional study, and the second was to verify that a small deviation from 0º incidence would create a wingtip vortex. The convergence of each solution was then verified. The convergence criterion previously noted was applied. It was found that all solutions at all angles of attack converged. A sample of a converged residuals plot is provided for the 3º angle of attack case in Figure 12 and shows the criterion for at least three orders of magnitude reduction in residuals was met. Figure 13 shows that the lift achieved a constant value after about 900 iterations whereas the drag reached a constant value before 200 iterations.

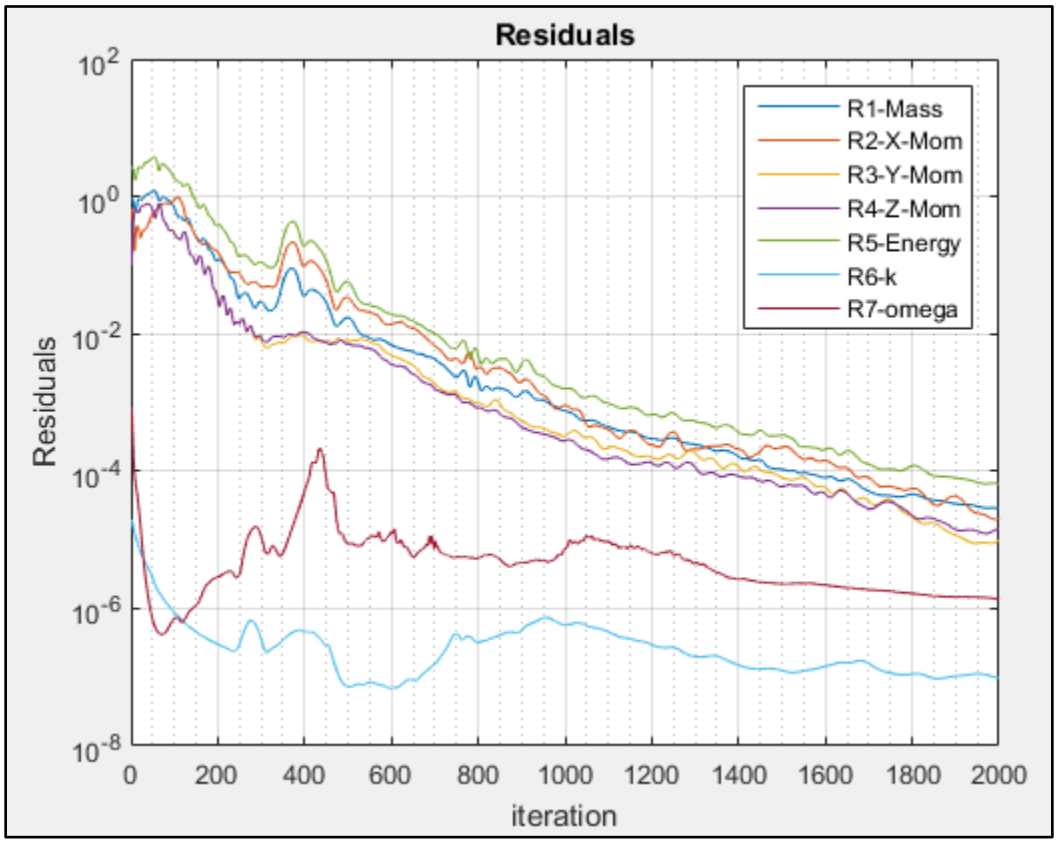

Figure 12: Residuals vs. Iteration for the 3º angle of attack finite wing case

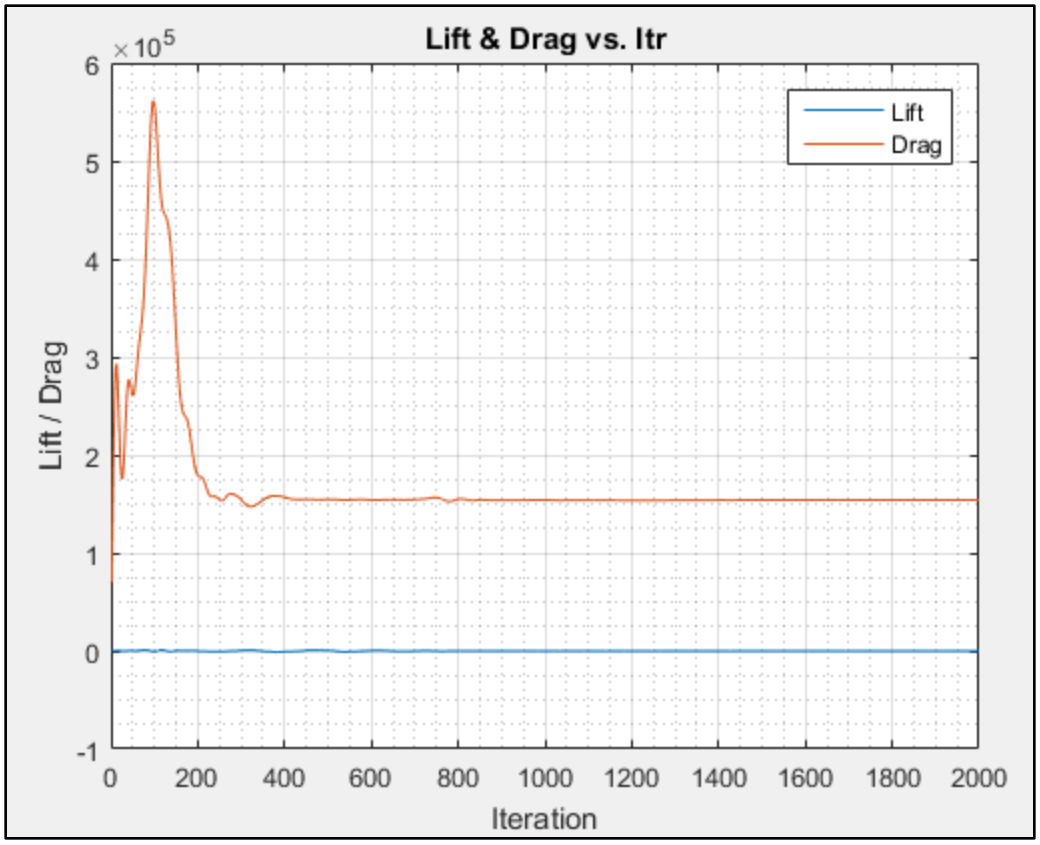

Figure 13: CL and CD vs. Iteration for the 3 finite wing case

With convergence confirmed, an additional step was taken to verify the data. Figure 14 and Figure 15 show the variation of lift and drag with angle of attack respectively. The present study does not deal with analyzing the forces of the wing; however, the data provided indication that results were reasonable. Specifically, for a wing with a symmetric airfoil, it is expected that:

- The relationship of lift with angle of attack should be linear (up to stall) and passes through zero lift at zero incidence
- The relationship of drag with angle of attack should be at a minimum at zero degree angles of attack, be of parabolic nature and be symmetric about zero incidence.

Figure 14 and Figure 15 clearly show that the aforementioned expected force relationships with angle of attack were satisfied. While force relationships are not a topic of the present study, this observation serves as further verification that the simulations are yielding reasonable results.

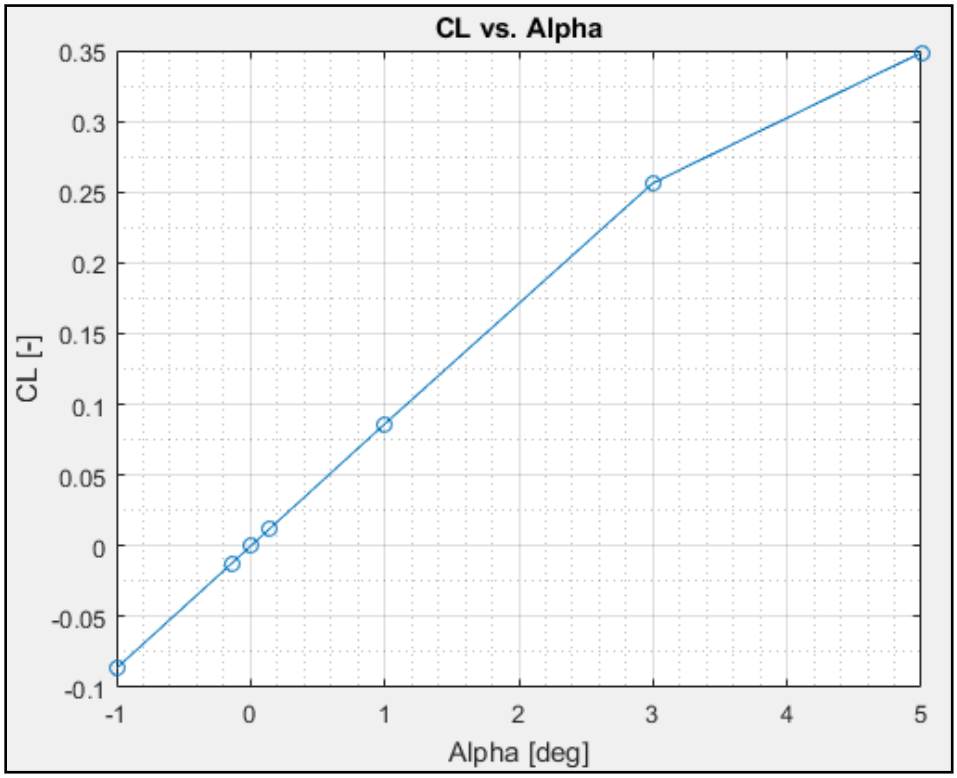

Figure 14: CL vs. Alpha for finite wing with NACA-0012 airfoil at Mach 0.758

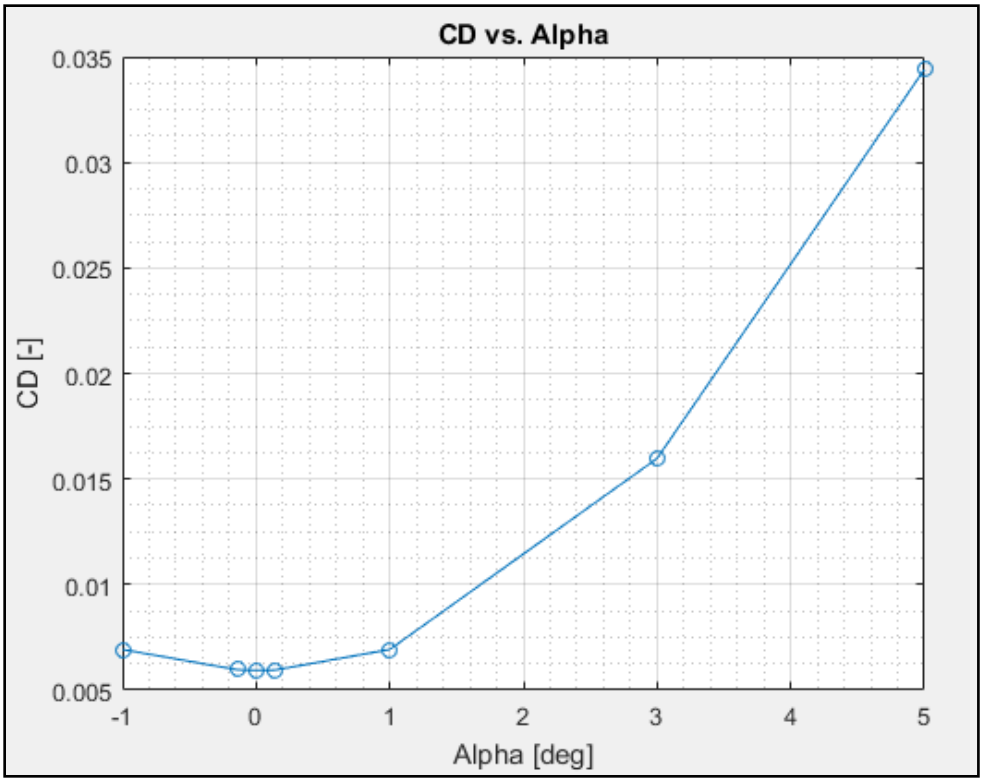

Figure 15: CD vs. Alpha for finite wing with NACA 0012 airfoil at Mach 0.758

The wingtip vortex is of interest in this study. Thus it is desirable to visualize vortex formation and evolution with angle of attack and attempt to understand its behavior with transonic shock interference. Figure 16.a-e. illustrate the skin friction lines along the wingtip surface with increasing angle of attack. The color contours indicate the surface pressure coefficient. The skin friction topology provides insight to the flowfield just above the surface [5]

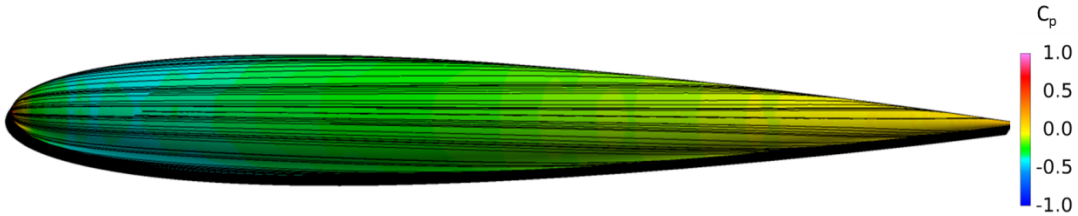

a: 0 incidence

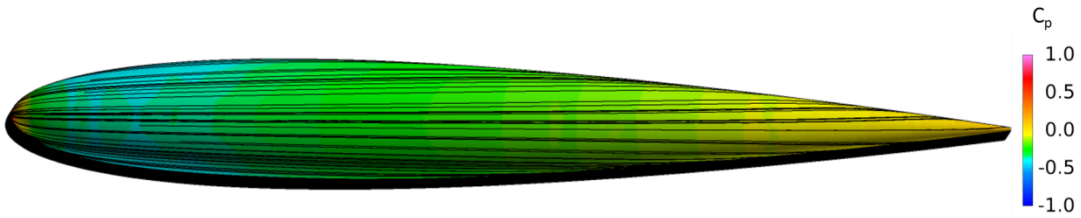

b: 0.14 degrees angle of attack

c: 1 degree angle of attack

d: 3 degrees angle of attack

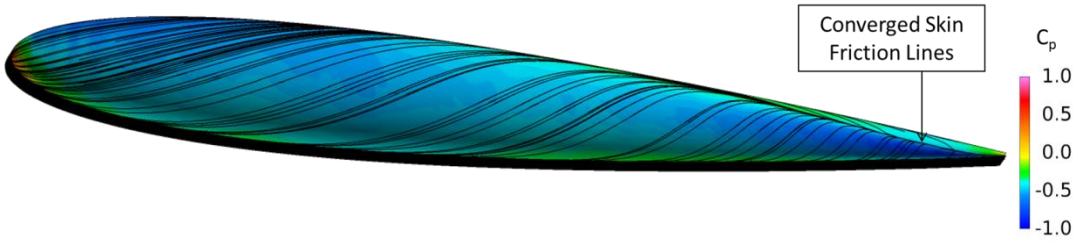

e: 5 degrees angle of attack

Figure 16: Skin friction lines on a finite wingtip

Looking at Figure 16.a., the skin friction lines run straight across the wingtip as to be expected since the airfoil is symmetric. At a small incidence of 0.14º, the skin friction lines start to show a slight deviation from symmetry. A slight rollup of skin friction lines from the lower to upper surface is observed from which one can infer the formation

of a weak wingtip vortex. It has been widely observed that in spite of shocks in the transonic range that wingtip vortices form in like manner as low-speed wings [6].

The rolling up of the skin friction lines from the bottom surface to the top surface becomes increasingly evident as the angle of attack is further increased. For example, Figure 16.d-e. show significant rollup. The convergence of skin friction lines indicated a line of open separation that is manifested as a vortex [5]. Further investigation of these phenomena using the Q-criterion, a standard vortex visualization method as described in [6], confirms that this rolling up of skin friction line is due to the presence of a wingtip vortex. This observation is presented in Figure 17 which includes a zoomed-in picture of the wing at 3º angle of attack and the Q-criterion illustrating the wingtip vortex in blue. It can be noted that the rolling up of the skin friction lines clearly corresponds with the vortex formation.

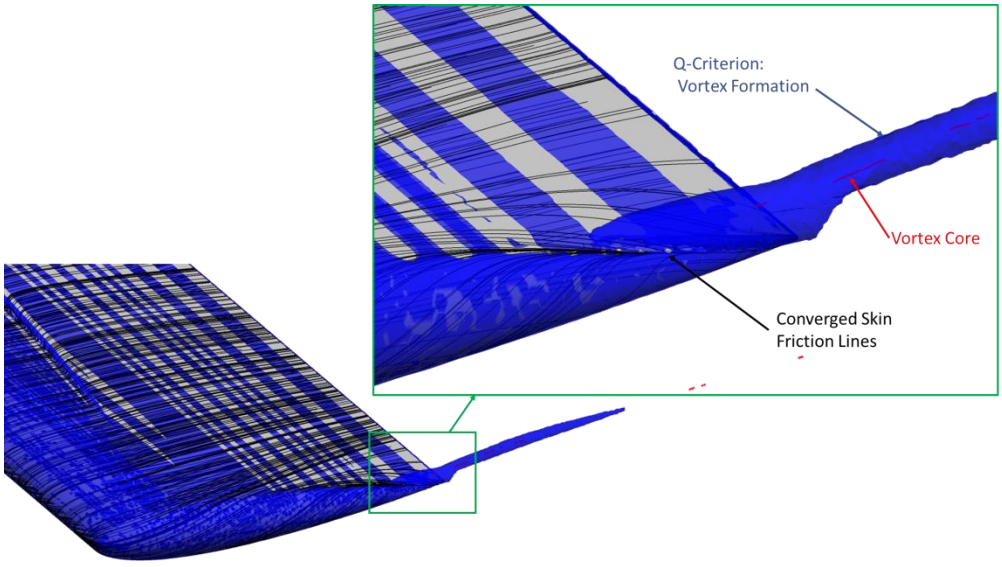

Figure 17: Q-Criterion illustrating wingtip vortex at 3º angle of attack

It is also desirable to observe the transonic shock wave formation. The present study attempts to observe how angle of attack influences shock wave location and its effect on the flowfield and surface topology. To visualize this, Figure 18.a.-e. present isometric views of the wing showing: surface C_p-distributions, surface skin friction lines as well as a section cut near the mid span of the wing plotting Mach distributions.

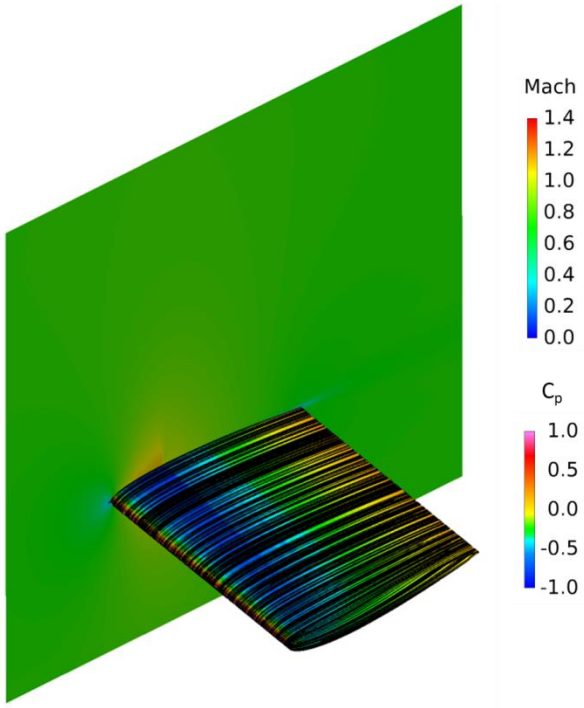

a: 0 incidence

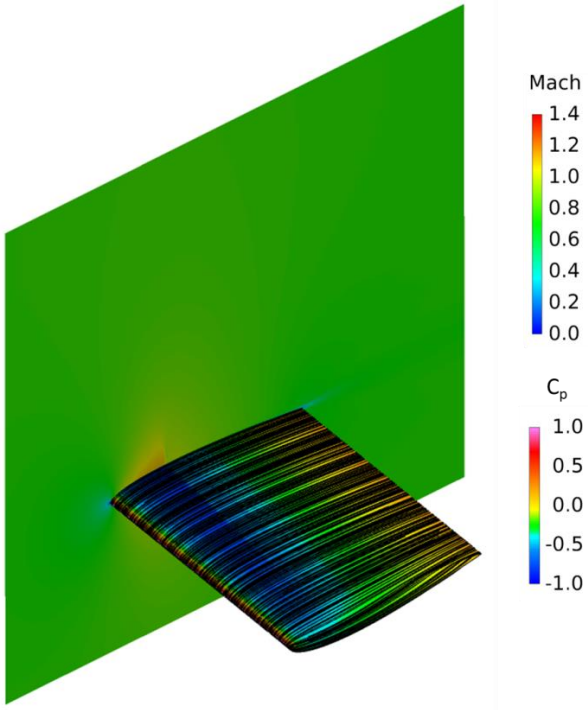

b: 0.14^{O} angle of attack

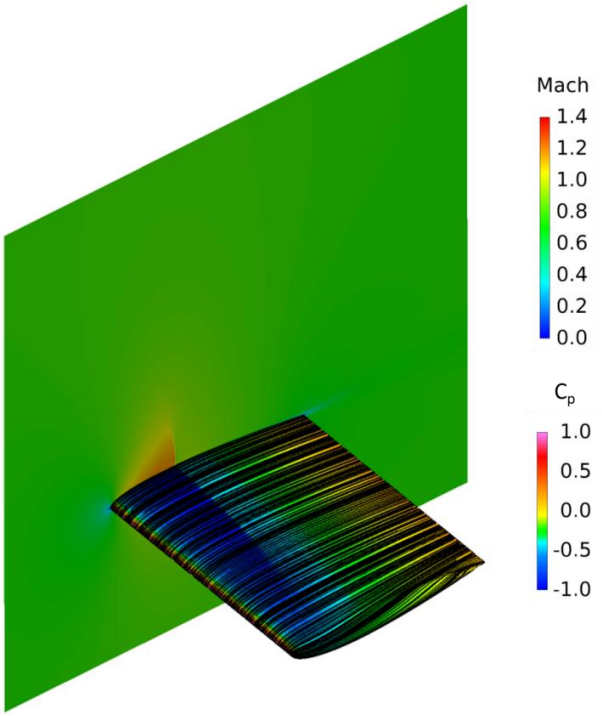

c: 1^{o} angle of attack

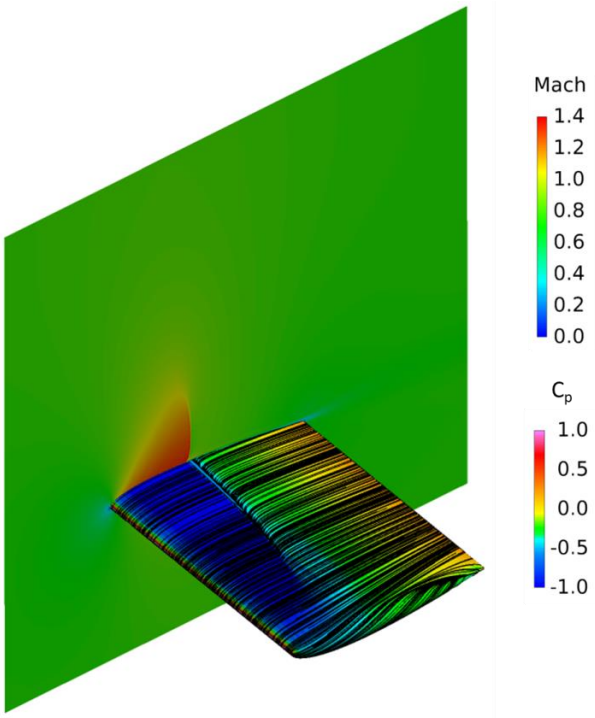

d: 3º angle of attack

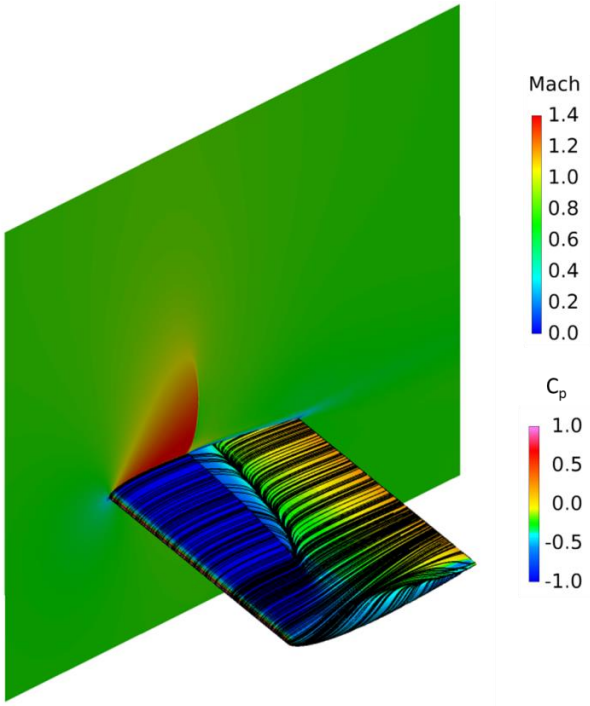

e: 5º angle of attack

Figure 18: Flow visualization of shock wave on a finite wing with a NACA-0012 airfoil at Mach 0.758

Figure 18 shows that at an incoming freestream Mach number of 0.758, a shock exists over the upper surface of the wing for all angles of attack, including zero incidence. As the angle of attack is increased the region of supersonic flow became more pronounced. Figure 18.d. shows that at 3º angle of attack the shock wave is strong enough to induce a small, visible separation zone. This is evident by examining the convergence of skin friction lines that is generally accepted to be evidence of three-dimensional separation [7]. For this angle of attack, the separation line is almost immediately followed by the reattachment line (made more clear in Figure 19.d). The proximity of the separation and reattachment lines indicates that the flow is just past incipient separation. Looking at Figure 18.e. it is now obvious that there exists a large shock-induced separation zone. This can be seen again through the skin friction lines, with the separation and reattachment lines now further apart.

To further investigate the skin friction lines and surface pressure distributions, Figure 19.a-e. show top-projected views of the wing at each angle of attack.

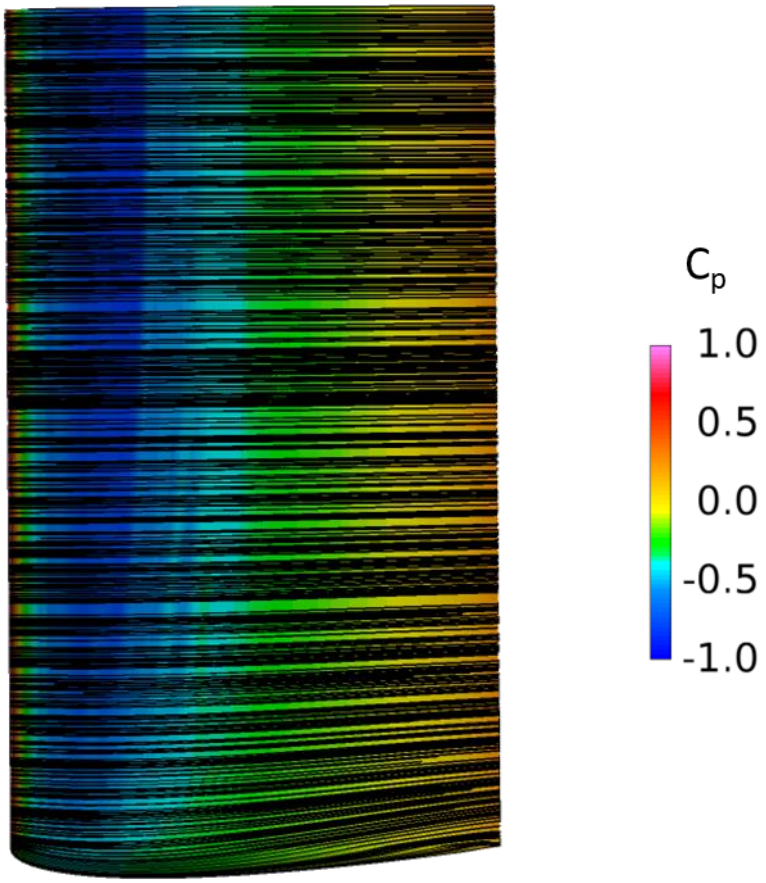

a: 0º incidence

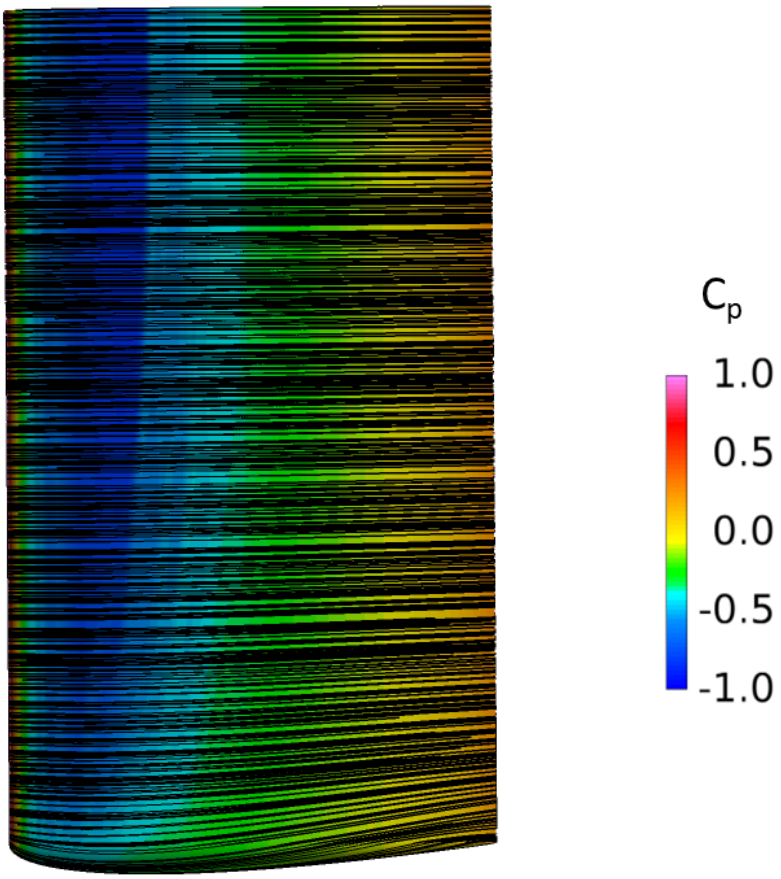

b 0.14º angle of attack

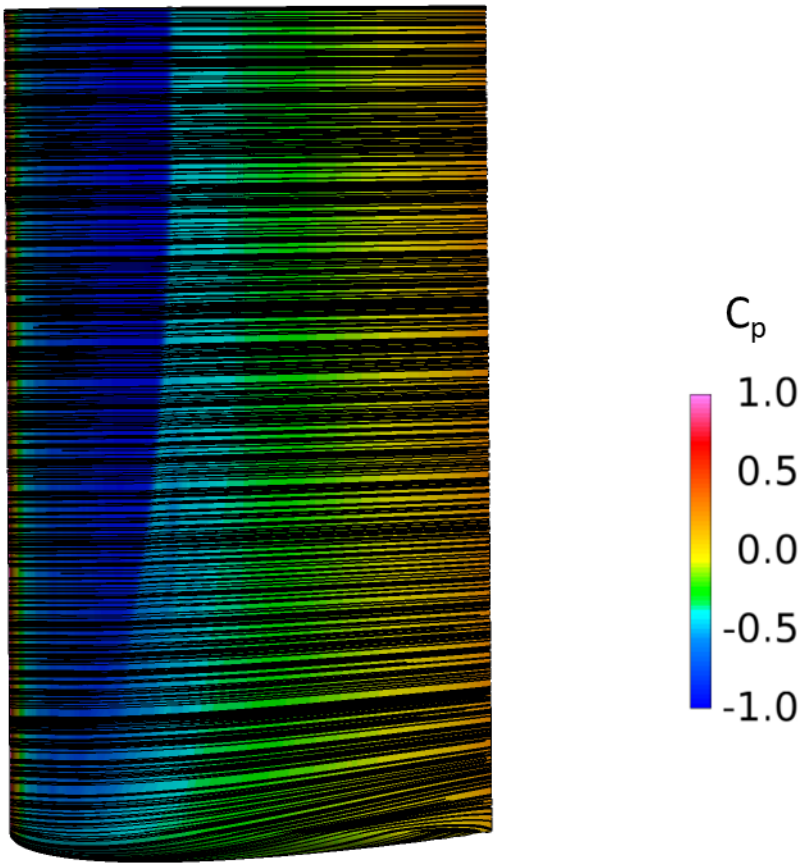

c: 1º angle of attack

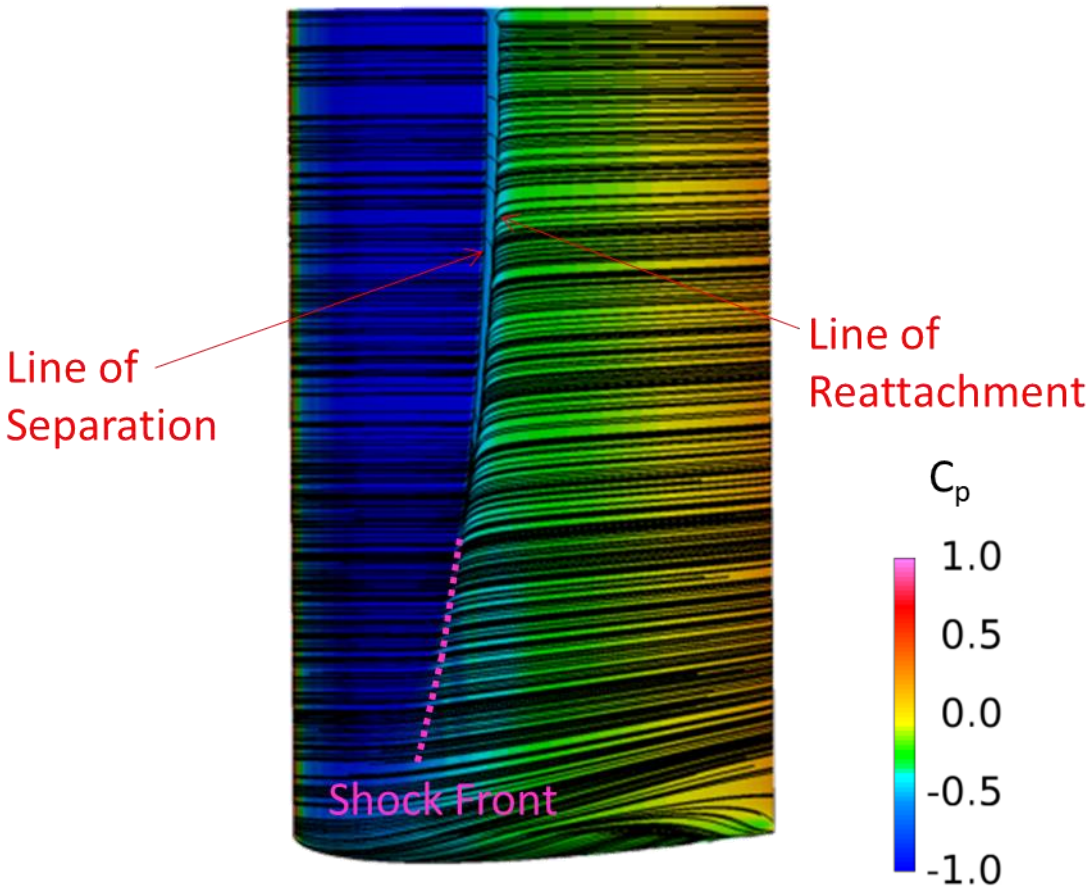

d: 3º angle of attack

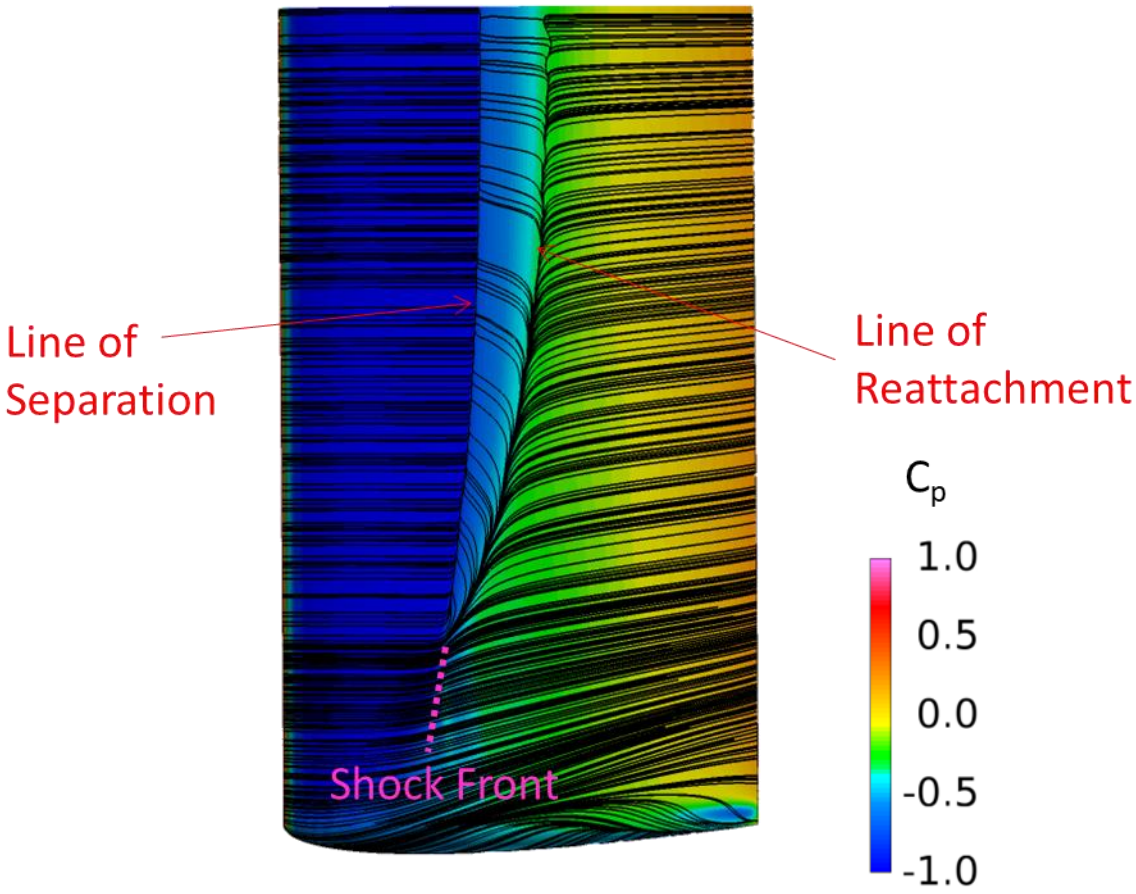

e: 5º angle of attack

Figure 19: Top view flow visualization of skin friction lines on finite wing with NACA-0012 airfoil at Mach 0.758

Figure 19 provides a clearer overview of the surface flow topology than shown in Figure 18. It is also possible to visualize the shock formation via Figure 19, even for the cases that separation did not occur, by keying into both the skin friction lines and the surface C_p-distributions. For the lower angle of attack cases, 0º, 0.14º and 1º shown in Figure 19.a-c. respectively, the shock front occurs right at the transition from dark blue to light blue on the C_p-distributions. Physically, this jump is the pressure rise across the

shock wave. Toward the outboard section of the 1º case in Figure 19.c. bending of the skin friction lines can be visualized right at the shock front, which is characteristic of skin friction lines passing a shock wave [7]. The shock front for the 3º and 5º cases in Figure 19d-e. is more apparent on the inboard section of the wing. The shock front can be visualized by the separation line, which is in fact created from the interaction of the shock with the boundary layer. As the separation line converges with reattachment line the shock front can still be visualized by observing the sharp bending of the skin friction lines. It can be noted that in Figure 19.d-e. the C_p-distributions near the wingtip have become complex compared to the inboard section of the wing. This is due to the complex pressure gradients present between the wingtip vortex and the presence of the shock.

Interesting observations can be made at both 3º and 5º angles of attack, where shock-induced separation is observed. In a two-dimensional case, the shock-induced separation would exist uniformly across the entire span of the infinitely long airfoil section. By introducing a finite wing, three-dimensional effects, in the form of wing tip vortex-shockwave interactions, become apparent. In both 3º and 5º degree angles of attack cases, the region of separation is larger near the root of the wing and tapers down to a termination point toward the wingtip. While the shock-induced separation is terminated, the shockwave itself continues moving outboard further towards the wing tip. This is clear evidence that, in some way, three-dimensional effects are preventing a uniform shock wave to be imposed along the span of the wing. It is believed that the wing tip vortex is acting to reduce the strength of the shock wave.

Perhaps the most interesting observation made regarding the surface flow topology occurs at the apex where the separation and reattachment lines converge.

Figure 19.e. has been zoomed in right at this apex in Figure 20 to further observe and discuss this flow topology feature

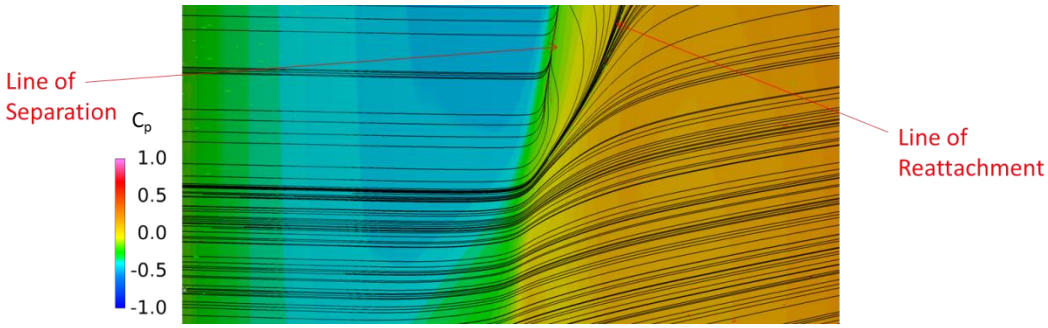

Figure 20: Zoomed in view of Figure R.e. right at the apex of separation and reattachment lines

It has been noted that convergence of the skin friction lines verified three-dimensional separation had occurred, however, different types of separation exist. Separated regions can be either open or closed, as described by K.C. Wang [10] (equivalent to local and global separation respectively as described by Peak and Tobak [7]). A region of open separation is not closed off to the freestream air, such that free stream air is able to leak inside the separated region. Regions of closed separation can be considered to be isolated to the freestream and are entirely self-contained. The criteria used to distinguish between open and closed separation regions is the presences of singular point(s) on the line of separation in which the skin friction lines emerge from. The line of separation for an open region of separation can be traced back to the initial line of attachment at the leading edge of the surface. The separation line for a closed region of separation originates and terminates at a singular point. In either case, a vortex of some sort is shed from apex of separation, further detail described by Wang [10]. In general, regions of open separation arise where significant cross flow is present. The main example presented in [10] is for flow around a body of revolution, another example is a swept wing. Observing this phenomenon on a straight wing may be counter-intuitive at

first, but after considering the cross flow imparted by the wing tip vortex this discovery makes sense.

From Figure 19.e. and Figure 20, it clear that the separated region is open as no singular point exists. In addition, the Q-criterion was utilized to visualize all vortices for the 5º angle of attack case and is shown in Figure 21. As previously noted, a vortex should be shed from the apex where the separation originates. Figure 22 does show clear evidence of a vortex being shed from the separation/reattachment apex. It is unclear why this vortex is not present in the solution. Some possibilities include: limitations of RANS solver and/or the scale on which the vortex exists may be so small that it is not being picked up in the flow visualization. This is a recommended area of future work and investigation.

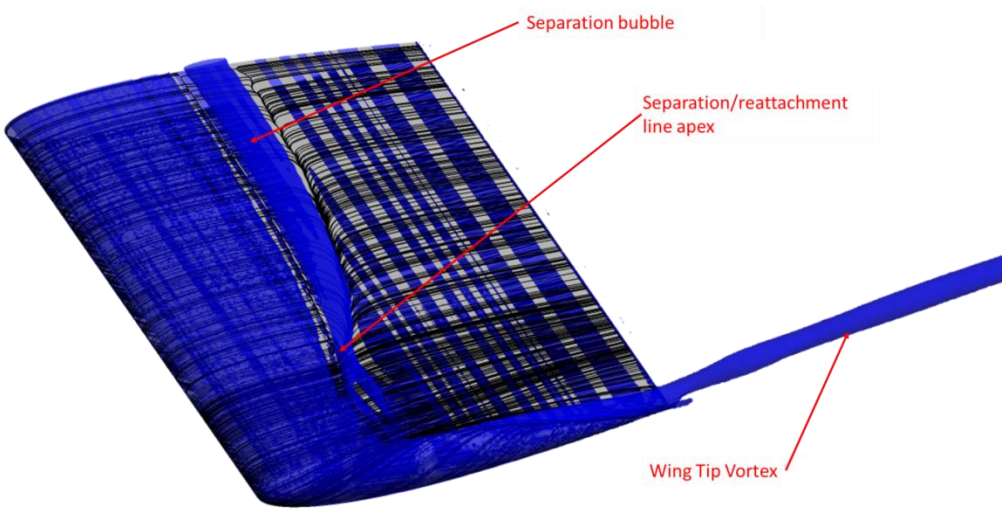

Figure 21: Q-Criterion flow visualization of a finite wing with NACA-0012 airfoil at Mach 0.758 at 5º angle of attack

Looking beyond the surface flow topology and into the outer flow around the wing some additional interesting observations were made. Again, the focus was on the 3º and

5º cases where shock-induced separation had occurred. Figure 22.a-j. and Figure 23.a-j. show cross-sectional cuts along the span of the wing at various percentage chord locations for the 3º and 5º case respectively. The view orientation for both Figure 22 and Figure 23 is looking aft and slightly downwards to see details on the wing upper surface. On these cross-sectional cuts, a contour mapping of the local Mach number is illustrated, as well as the v-w velocity component vector in the same plane. A sonic line is included to give a clear depiction of both the supersonic and subsonic regions of flow. This gives a detailed mapping of the velocity vector across the entire wing at various chord wise locations.

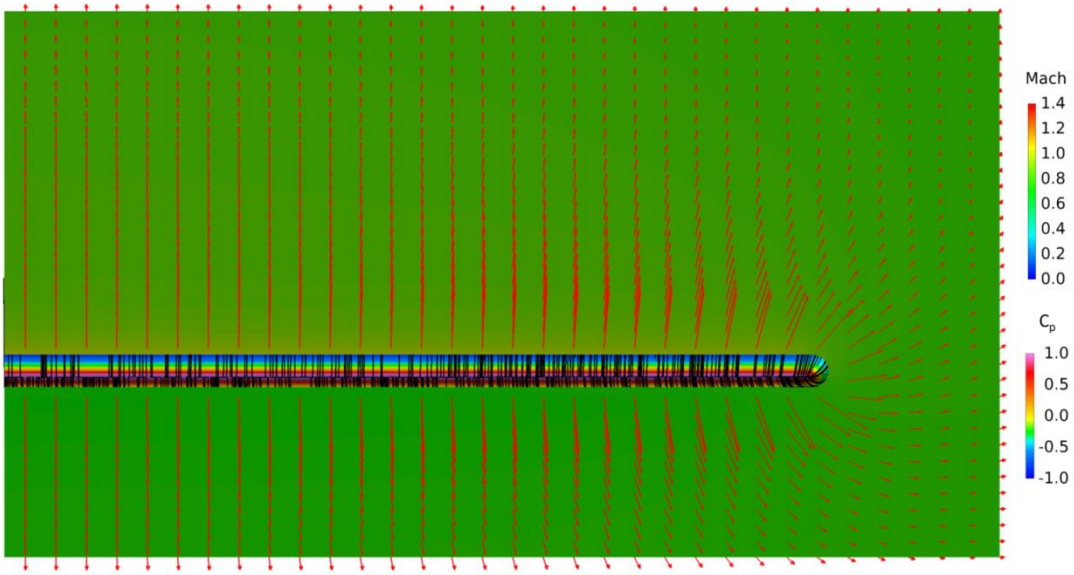

a: 5% chord

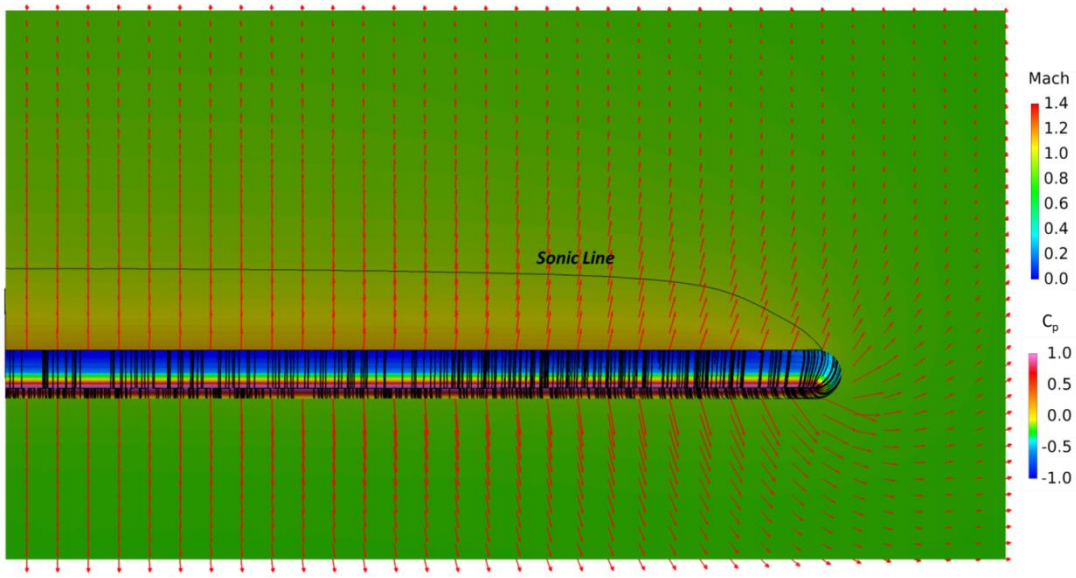

b: 13% chord

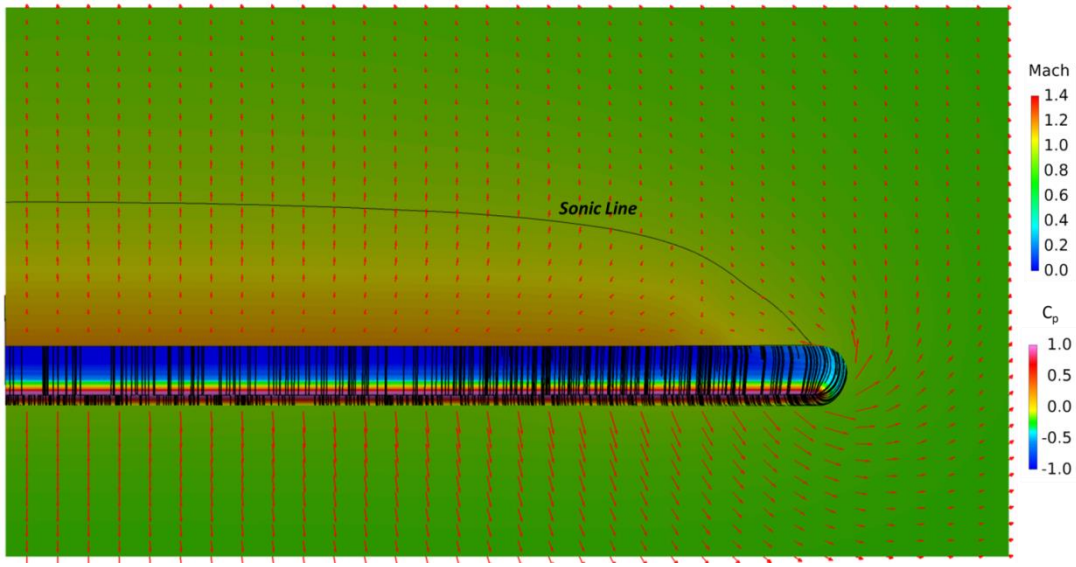

c: 21% chord

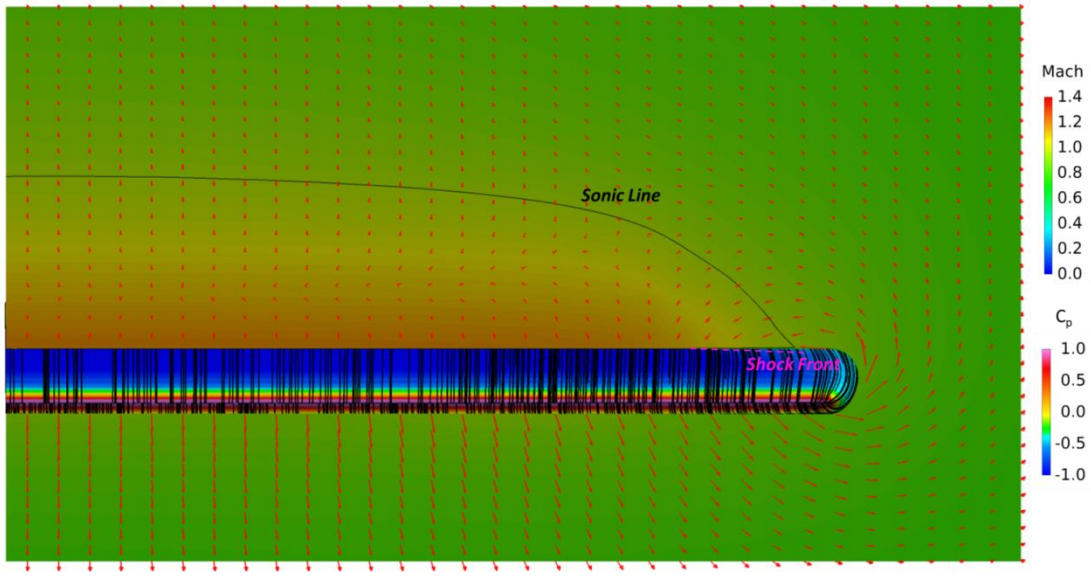

d: 25% chord

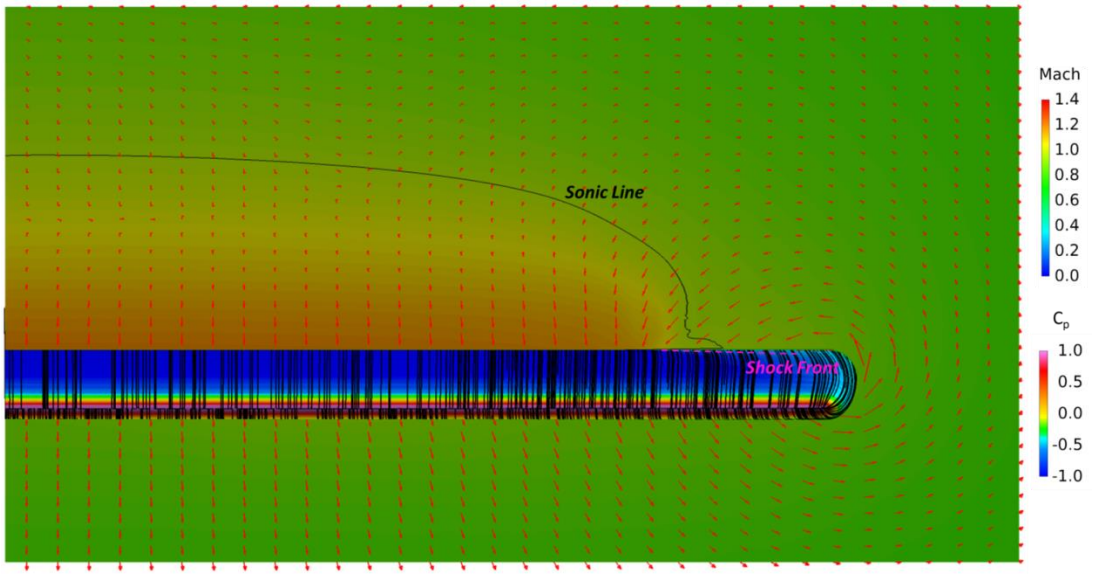

e: 29% chord

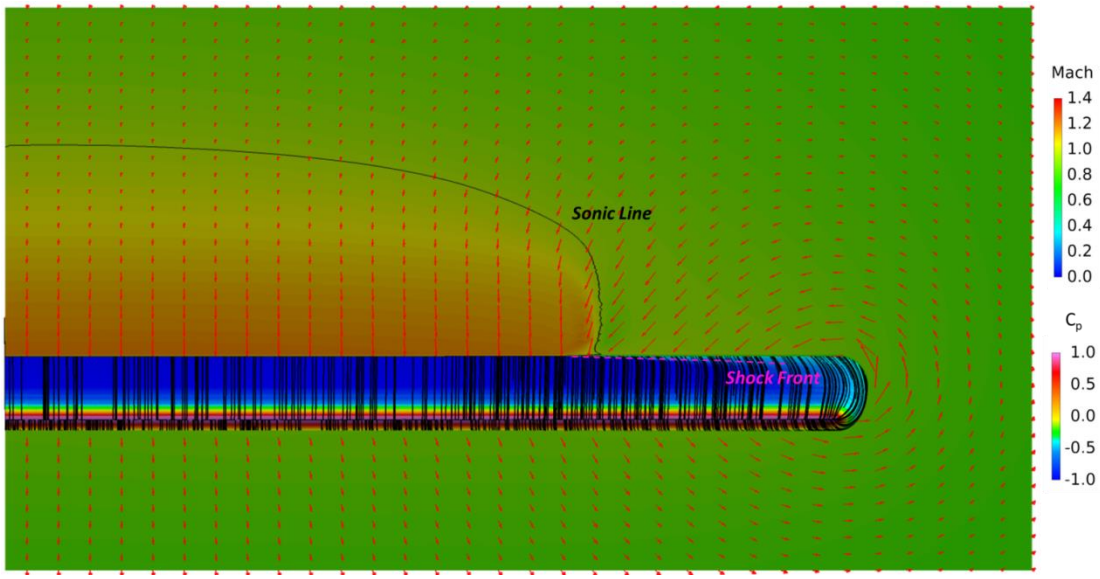

f: 33% chord

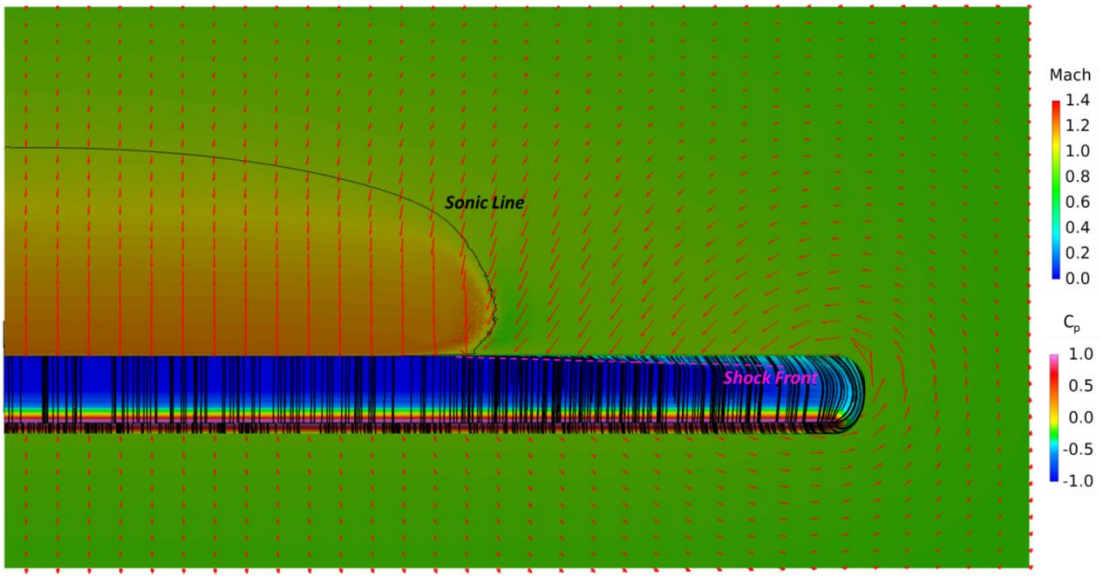

g: 37% chord

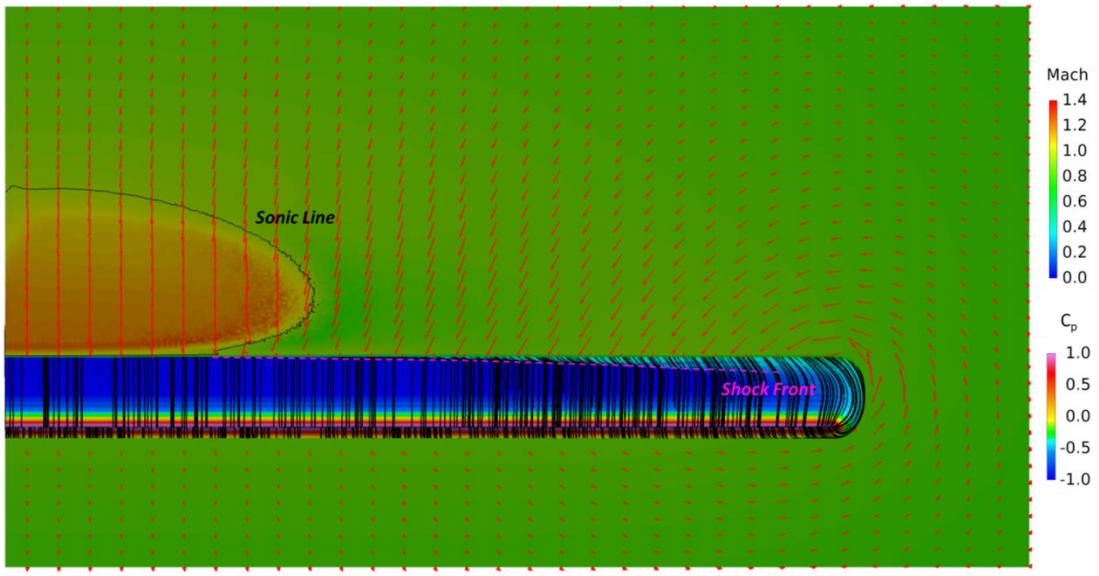

h: 41% chord

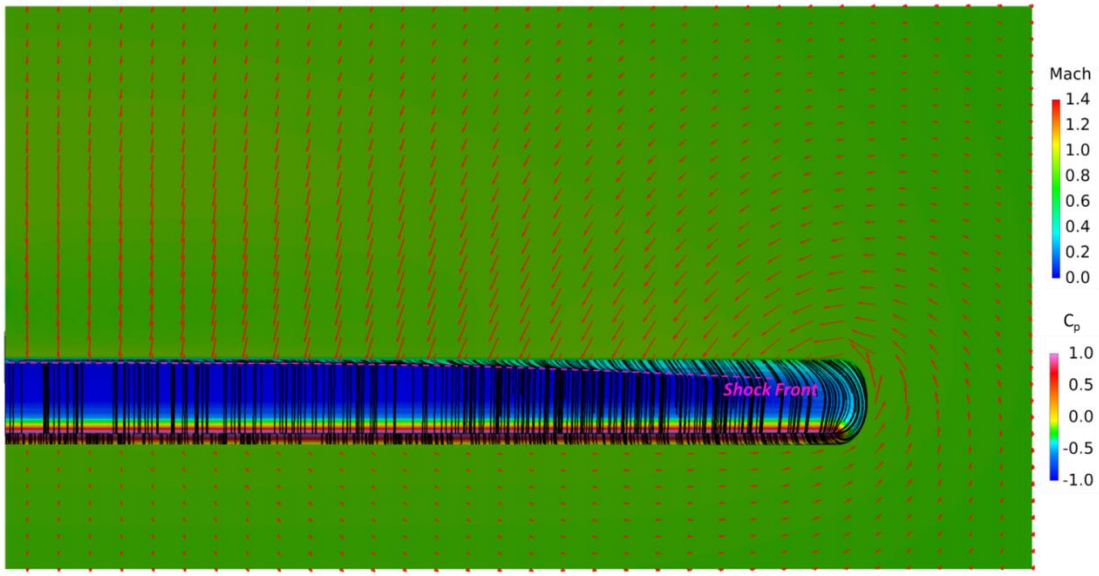

i: 45% chord

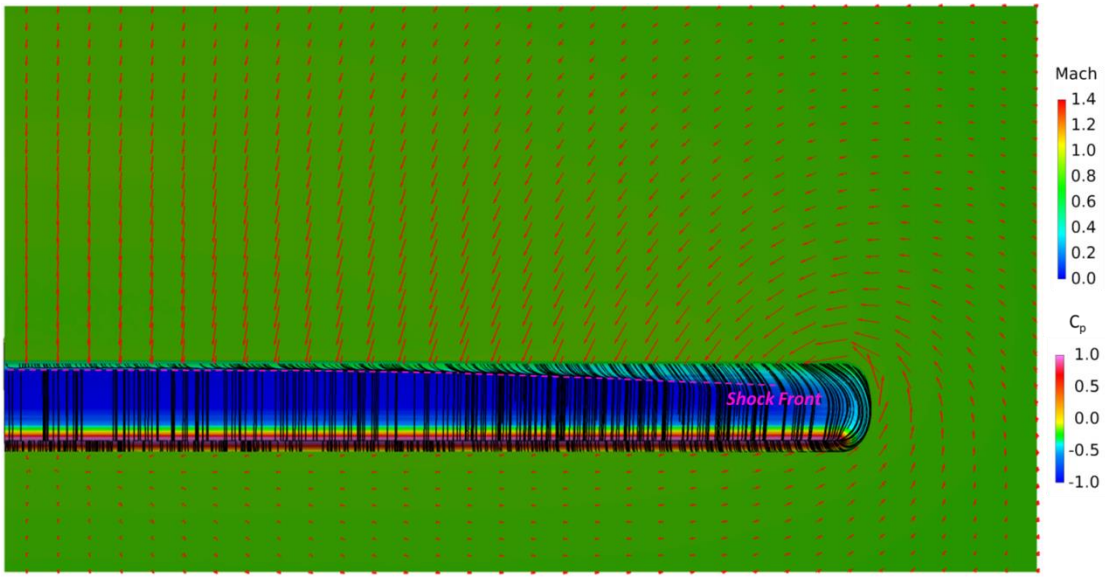

j: 49% chord

Figure 22: Spanwise cross-sectional cuts showing local Mach and velocity components for a finite wing with NACA-0012 airfoil at Mach 0.758 at 3º angle of attack

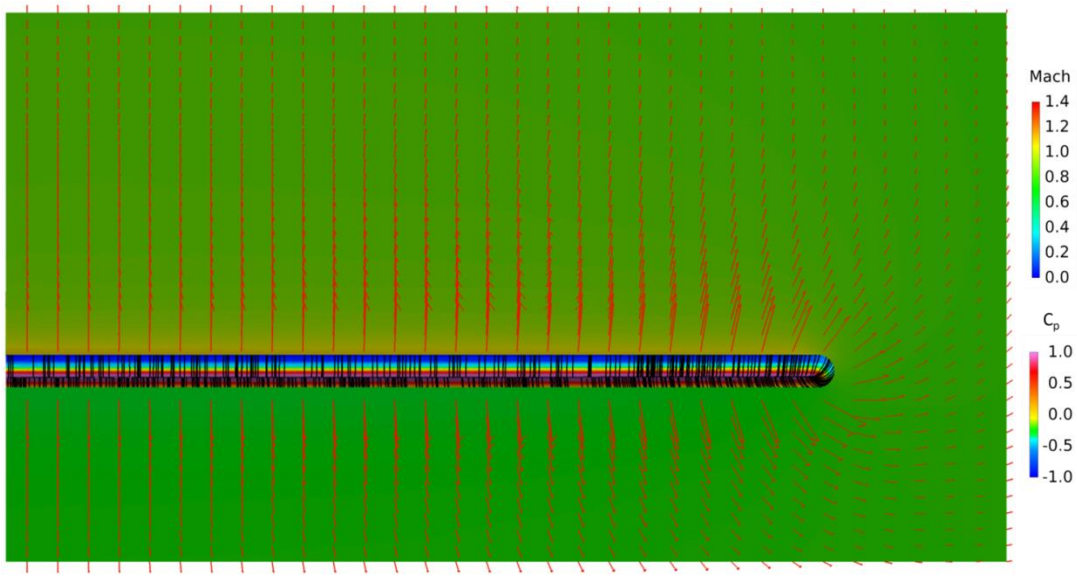

a: 5% chord

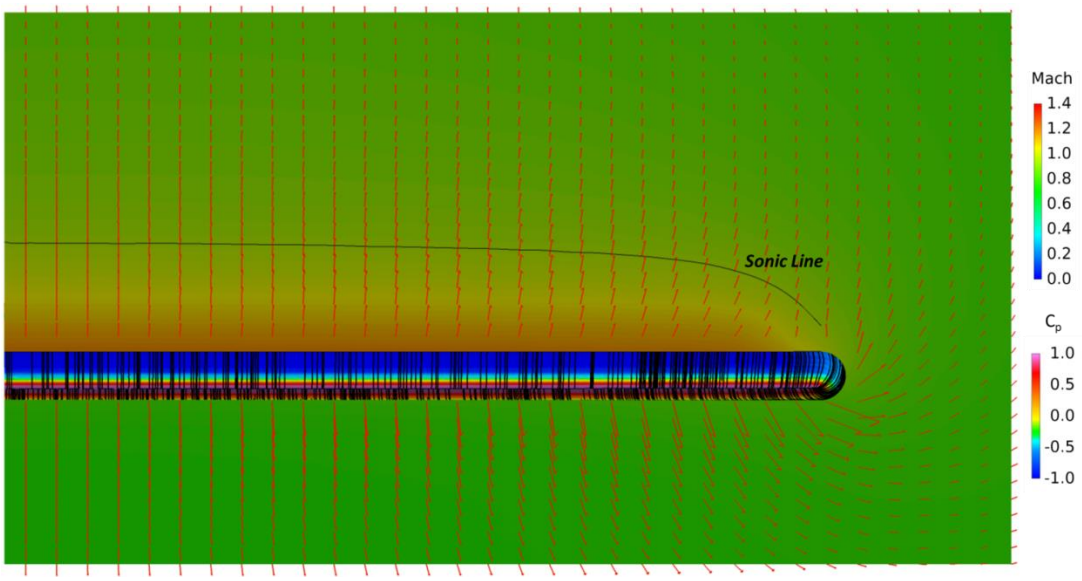

b: 13% chord

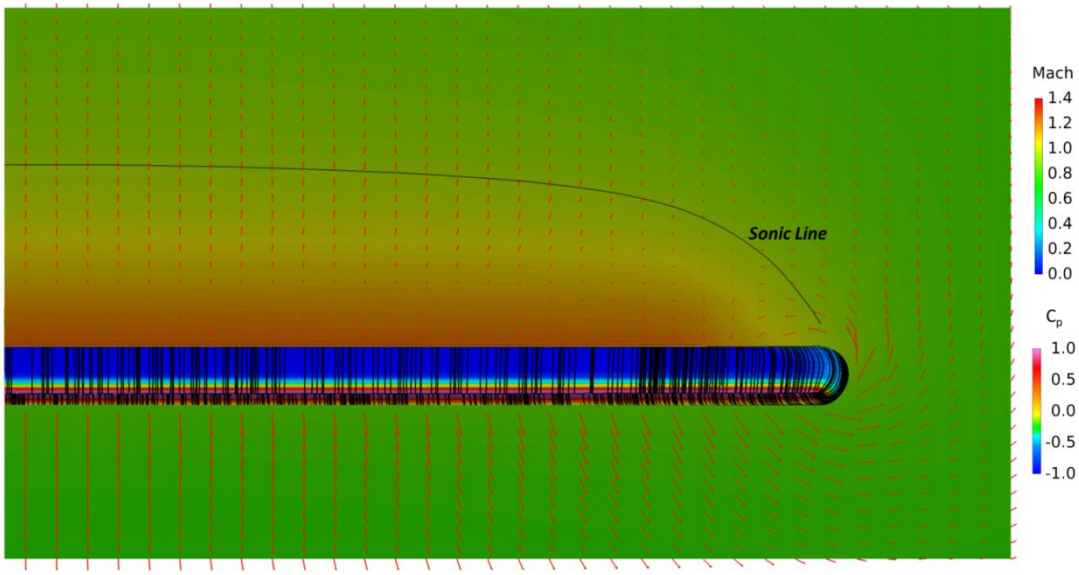

c: 21% chord

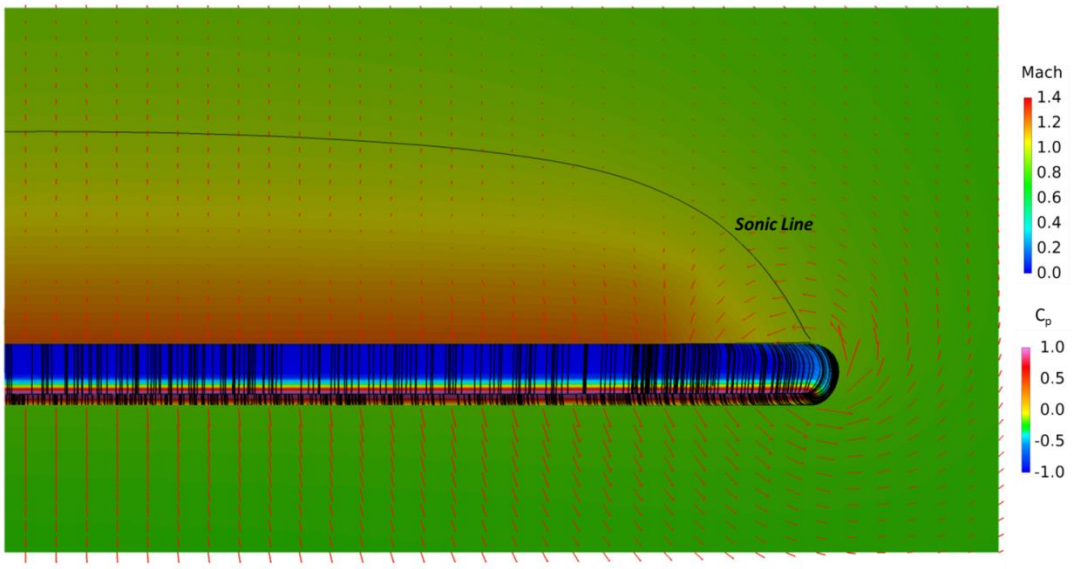

d: 25% chord

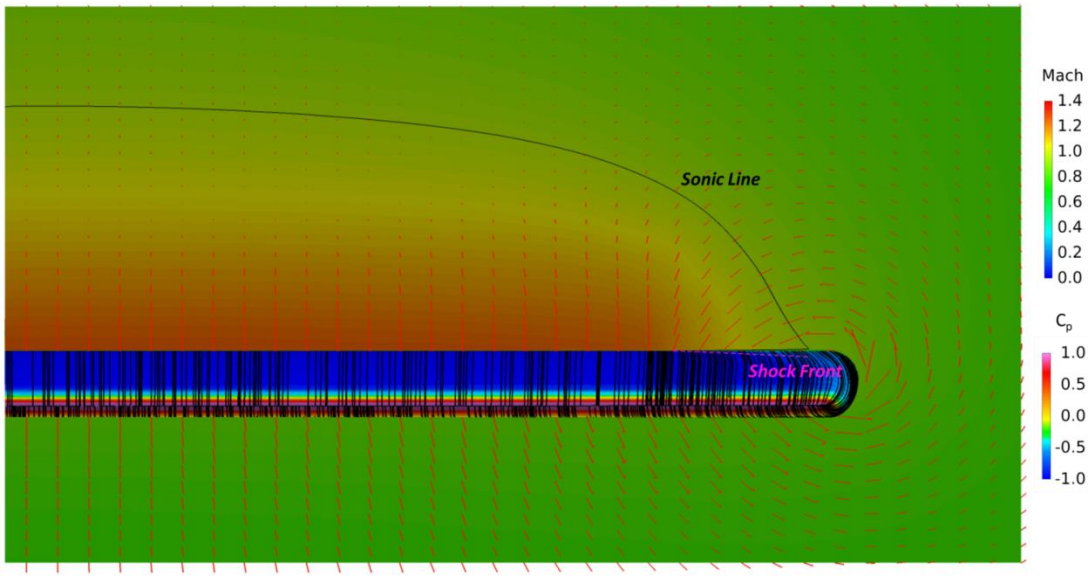

e: 29% chord

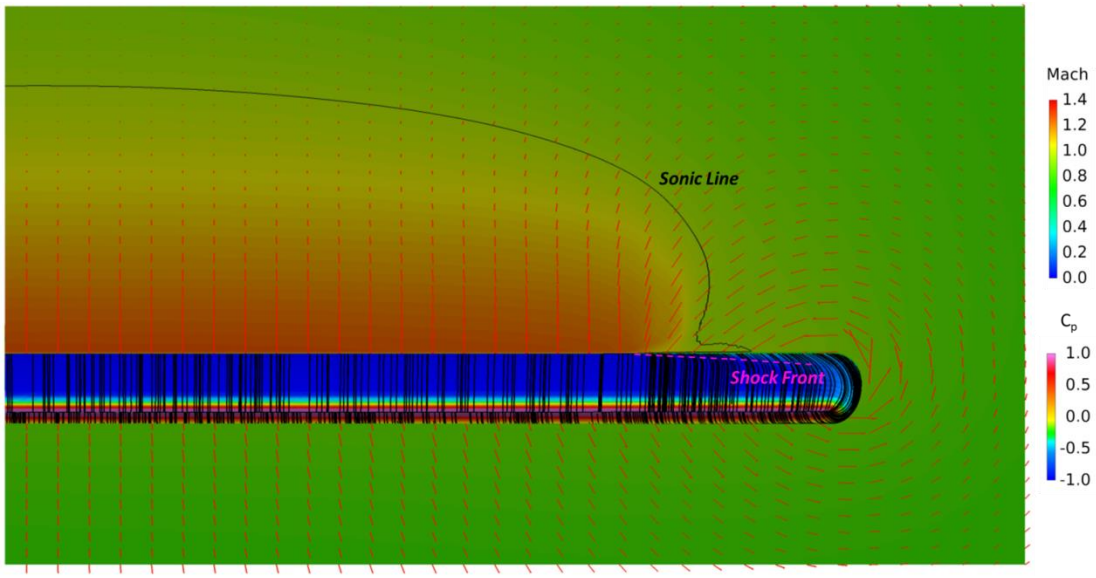

f: 33% chord

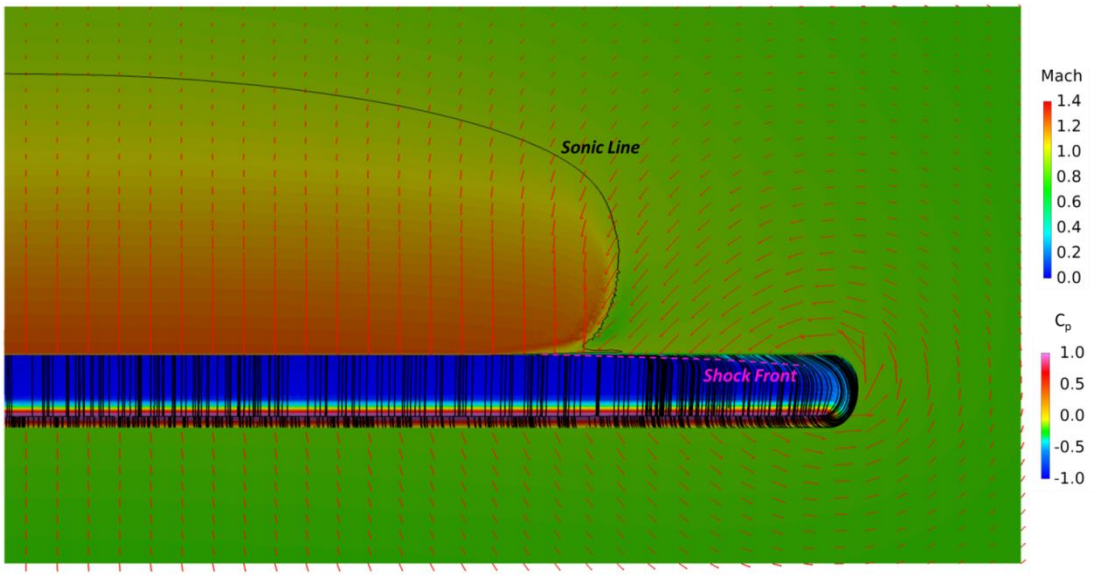

g: 37% chord

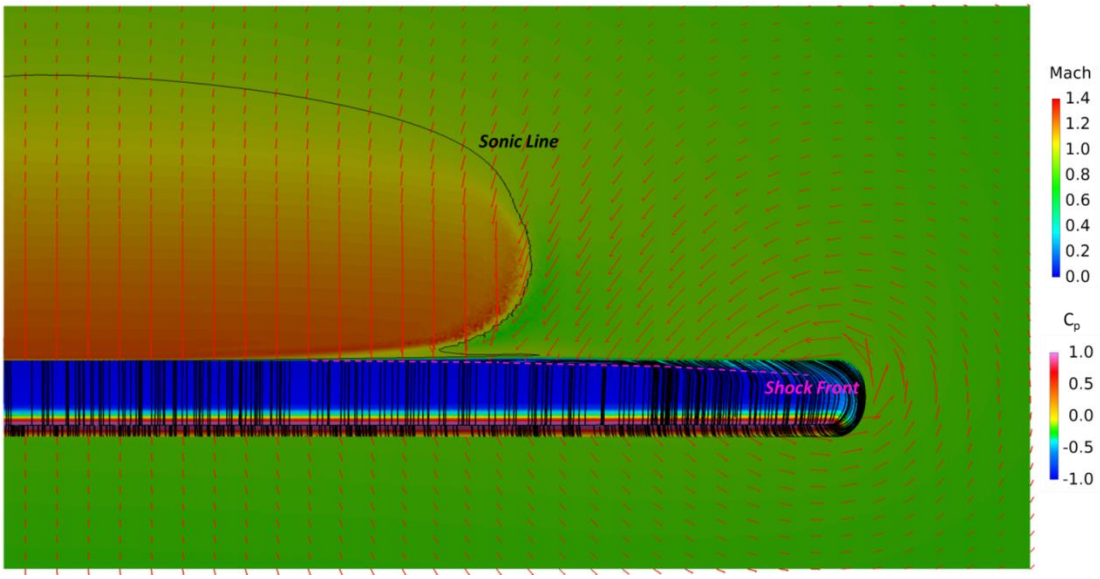

h.: 41% chord

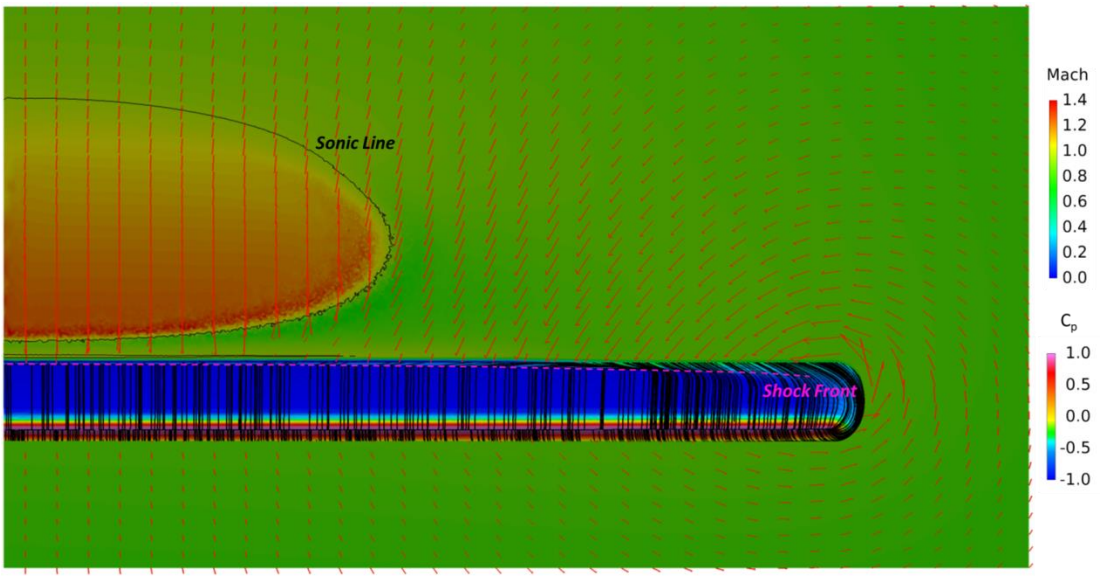

i: 45% chord

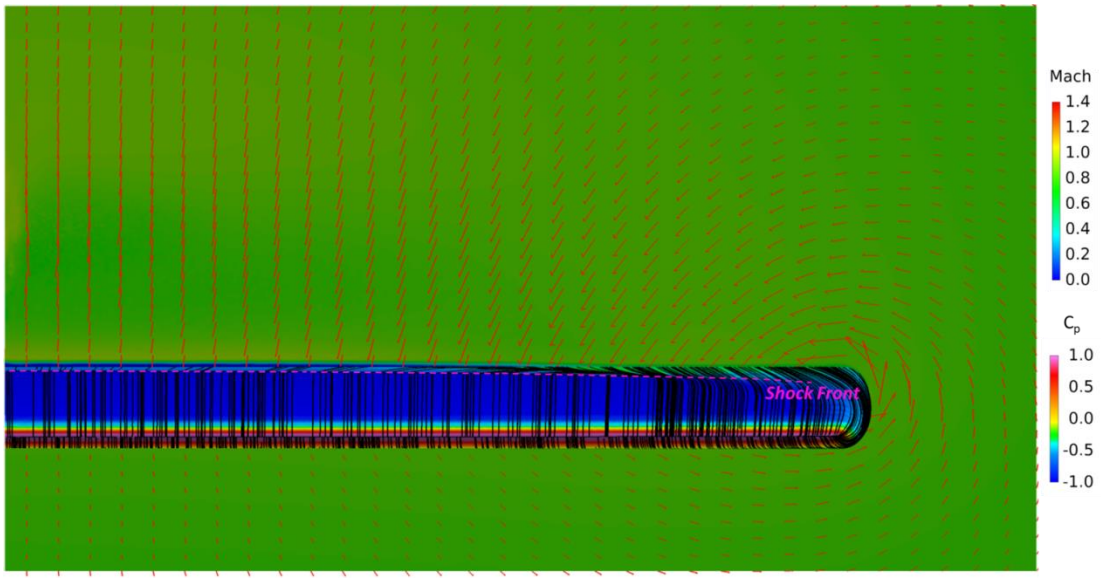

j: 49% chord

Figure 23: Spanwise cross-sectional cuts showing local Mach and velocity components for a finite wing with NACA-0012 airfoil at Mach 0.758 at 3º angle of attack

Figure 22 and Figure 23 present a unique flowfield. In either case, as one advances down the chord of the wing, there exists a region of high axial velocity component (high local Mach number). Stepping through the 3º case in Figure 22, Figure 22.a-c. show no distinct interaction between the wingtip vortex and the shock wave. It can be seen that the axial velocity is increasing as it accelerates over the wing's upper surface. It is also clear through the v-w velocity vectors that the wing vortex has begun to form. In Figure 22.d. it is clear that there are two distinct flow regimes present. The first regime is the area being affected by the wingtip vortex with lower axial velocities and significant spanwise flow (referred to as regime one); the second regime is the area unaffected by the wingtip vortex with significantly higher axial velocities and no spanwise flow (referred to as regime two). These two regimes appear to be distinct and an

explanation will be provided below. It can be noted that the shock wave front in Figure 22 (and Figure 23) is a curved shock due to three-dimensional effects. Figure 22.f-h. show that the delineation between the two defined flow regimes is in fact where the shock front crosses through the respective cross-sectional cut. The shock is able to intersect the spanwise cross-sectional cuts because of its curved nature. A two-dimensional shock wave would run parallel to these cross-sectional cut planes and this phenomenon would not be possible.

It can be noted that a third regime of flow could be considered to be the boundary layer flow. This would also encompass the SBLI region. While this regime is of the utmost importance to this analysis, as it is a key element of how the shock wave takes form, the observations made in the present study are concerned with the flow outside of this boundary layer and the surface flow topology.

In general, the sonic lines shown in Figure 22 can be considered to delineate the two defined flow regimes. This observation breaks down in some cases, specifically Figure 22.e., it is assumed this is due to the complex flow near the surface and small deviations in Mach number. In Figure 22.i-j. the flow has decelerated over the upper surface and is entirely subsonic, thus the entire flowfield can be considered to be regime one. The observation also breaks down for cross-section cuts upstream of the shock front.

Figure 23 shows the same general results as Figure 22. An interesting observation that is specific to the Figure 23 can be observed in Figure 23.i. The supersonic region appears to hook inward as the wing surface is approached. This is easily understood by observing Figure 23.i. from an isometric perspective and including

some chord-wise cross-sectional cuts along the span of the wing. This is shown in Figure 24 below.

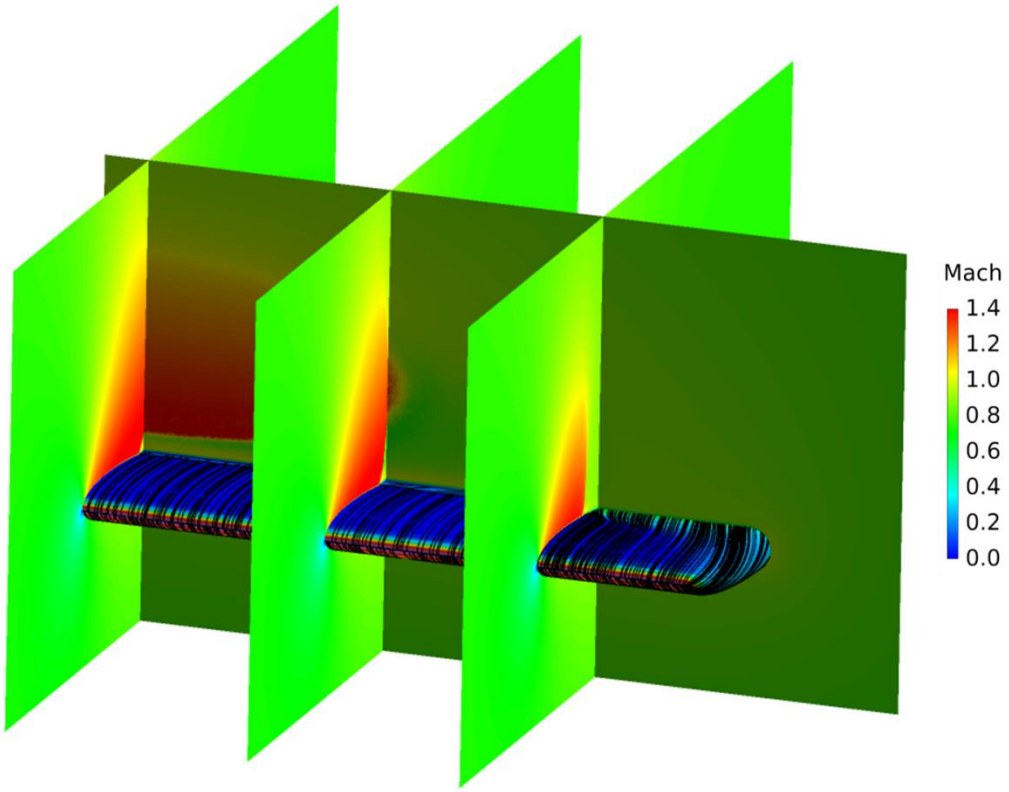

Figure 24: Isometric view of Figure 24.i with various chord-wise cross-sectional cuts along the wing span

It is clear that the shaping of the supersonic region in both Figure 23.i. and Figure 24 is due to the three-dimensional nature of the shock wave. The shock wave has a complex curvature, in that the shock wave itself is curved as it emanates outward from the wing surface and the shock front is curved, it moves closer to the leading edge as it moves outboard on the wing. The outboard-most chord-wise cut plane of Figure 24 shows that the shock's effect is such that the entire shock structure is forward of the

spanwise cut plane at 45% chord. The shock's effect in the inboard-most chord-wise cut plane of Figure 24 is such that the shock front is forward of the 45% chord plane, but the shock structure itself passes through said plane. The center chord-wise plane of Figure 24 is similar to the inboard plane, except the shock front is further forward, which causes the shock structure to intersect higher up on the 45% chord plane. The combination of these three chord-wise cross-sectional planes is what creates the unique flow pattern observed in Figure 23.i.

It can be noted that, in Figure 23.i. the observations made in Figure 22 still hold true. The supersonic region enclosed by the sonic line is acting as regime two, with no influence from the wingtip vortex. Outside of the sonic line, the rest of the flow is affected by the wingtip vortex. It can even be seen that the vortex is having an effect on the region between the supersonic bubble and the wing upper surface.

These observations can be further enforced by examining the asymmetry in the v-w velocity vectors between the upper and lower side of the wing. For example, Figure 22.f. shows that at approximately the wings mid-span, above the wing, the flow can be categorized in regime two whereas below the wing it is clear the wingtip vortex is having influence on the flow field which categorizes it into regime one. The difference between the upper and lower portions of the wing arises from the magnitudes of axial velocities and thus local Mach number. The flow below the wing is entirely subsonic whereas the above the wing surface there exists supersonic flow and thus regime two flow.

Figure 22 and Figure 23 confirm that there is a distinct interaction between the wing tip vortex and transonic shock wave. This interaction is directly related to the local Mach number. These results pose an interesting question: is the effect of the wingtip

vortex in regime one preventing the expansion of higher Mach flow in regime two, or vice-versa?

Chapter 4 : Conclusions and Recommendations for Future Work

The present study provided a qualitative analysis on the interaction between a shockwave and wingtip vortex in transonic flow. The results showed very complex surface flow topology once the shockwave was strong enough to produce shock-induced separation. This surface flow topology was such that the region of separation terminated before reaching the wingtip. Due to the absence of a singular point in the flow topology this separated region was considered to be an open. A distinct interaction in the flow exterior to the boundary layer was observed. The results showed two distinct regions of flow: one with very high axial velocities that was unaffected by the wingtip vortex, and another of lower axial velocities that was heavily influenced by the wingtip vortices. In general, these two regions of flow were delineated by the sonic line, such that supersonic regions and subsonic regions were behaving separately. A third region of flow was also considered to be the boundary layer and SBLI regions. This third region was not examined in detail in the present study, however, it is noted that it has great influence on both surface flow topology and the flow exterior to the boundary layer.

There are many directions in which future work on this topic could be taken. The first route would be continuing the pure fluid dynamics research path. One question remained unanswered in the present study is where is the vortex being shed from the separation/reattachment apex. A detailed investigation of the nature of this separated region in general would be a natural next-step for this study. Additional research, both experimentally or numerically can be done to further explore this discovery. The other path for future work on this topic is the applied research route. Both the creation and prevention of vortex formation in aerospace engineering is very common. Observations made on the interaction between vortices and shock waves could prove to be significant for specific engineering applications.

Appendix A

Student Access to Pointwise and TACC Resources

Pointwise:

Gaining Access:

- Install VPN
  - A VPN is required to access certain university resources including Pointwise.
  - Go to:
    - http://www.uta.edu/oit/cs/software/vpn/index.php .
  - Follow website instructions for setting up a VPN.
- Download Pointwise
  - Download most recent version from Pointwise website http://www.pointwise.com/downloads/
    - A license manager is not required, download and install pointwise software only
- Obtain License Server from UTA
  - Work with your thesis advisor to find the point-of-contact (POC) for receiving a License Server number
- Run Pointwise software with new license server
  - Run Pointwise software – it will prompt an error stating no license was found
  - Click “OK”
  - Select “Specifiy License Server”
  - Enter License Server
  - Finish

Texas Advanced Computing Center (TACC):

Gaining Access:

- Request Access
  - Go to TACC user portal website: https://portal.tacc.utexas.edu/home
  - Select “Create a TACC Account”
  - Read and agree to the TACC Acceptable Use Policy
  - Fill out the requested information to request your account
  - You will receive a confirmation email regarding your request
  - You will then receive an acceptance email regarding your request
    - This message will contain the required links to activate our account as well as where to find user guides for TACC resource

References

[1] R. Vieira, J. Azevedo, “RANS Simulations of Flows with Shock Wave-Boundary Layer Interaction,” *AIAA Paper 2013-0985*,pp. 41

[2] R. Biedron et al., “FUN3D Manual 13.2,” *NASA Technical Memorandum 2017-219661*, pp. 17, 2017

[3] C. Harris, “Two-Dimensional Aerodynamic Characteristics of the NACA 0012 Airfoil in the Langley 8-Foot Pressure Tunnel,” *NASA Technical Memorandum 81927*, 1981

[4] C. Brooks, C. Harris, P. Reagon, “The NASA Langley 8-Foot Transonic Pressure Tunnel Calibration,” *NASA Technical Paper 3437*, 1994

[5] J. Hunt, C. Abell, J. Peterka, H. Woo, “Kinematic Studies of the Flows Around Free or Surface-Mounted Obstacles; Applying topology to Flow Visualization,” *Journal of Fluid Mechanics Volume 86 Issue 1*,pp. 179-200, 1978

[6] V. Holmen, “Methods for Vortex Identification,” pp. 13

[7] D. Peake, M. Tobak, “Topology of Three-Dimensional Separated Flows,” *NASA Technical Memorandum 81294*, 1981

[8] F. Owen, A. Owen, “Measurement and Assesment of Wind Tuennel Flow Quality,” Progress in Aerospace Sciences, Volume 44, Issue 5, pp. 315-348, 2008

[9] K. Fujii, “Progress and Future Prospects of CFD in Aerospace – Wind Tunnel and Beyond,” Progress in Aerospace Sciences, Volume 41, Issue 6, pp. 455-470, 20015

[10] K. C. Wang, “Spearation of Three-Dimensional Flow,” pp. 11-16 1976

Biographical Information

I received my undergraduate degree in aerospace engineering from Penn State University in 2013. During my time at Penn State I took an engineering co-op working at US Airways in Pittsburgh Pennsylvania. During that co-op I gained a great appreciation for the aerospace industry. After graduating, I took a job at Bell in 2014 as an airframe design engineer working on the V-280 Valor Program. During my time as an airframe designer, I enrolled at UTA to pursue a Master's degree in Aerospace engineering to better prepare myself for a career in aerodynamics. I have since moved on to working in Bell's Advanced Tiltrotor Systems department as an Aerodynamics Engineer. The primary role of my job is conducting CFD analysis.